COOL CORE CYCLES: COLD GAS AND AGN JET FEEDBACK IN CLUSTER CORES

DEOVRAT PRASAD[1], PRATEEK SHARMA[1], AND ARIF BABUL[2]
[1] Joint Astronomy Program and Department of Physics, Indian Institute of Science, Bangalore, 560012, India;
deovrat@physics.iisc.ernet.in, prateek@physics.iisc.ernet.in
[2] Department of Physics and Astronomy, University of Victoria, Victoria, BC V8P 1A1, Canada; babul@uvic.ca

ABSTRACT

Using high-resolution 3D and 2D (axisymmetric) hydrodynamic simulations in spherical geometry, we study the evolution of cool cluster cores heated by feedback-driven bipolar active galactic nuclei (AGNs) jets. Condensation of cold gas, and the consequent enhanced accretion, is required for AGN feedback to balance radiative cooling with reasonable efficiencies, and to match the observed cool core properties. A feedback efficiency (mechanical luminosity $\approx \epsilon \dot{M}_{acc} c^2$; where $\dot{M}_{acc}$ is the mass accretion rate at 1 kpc) as small as 6×10^{-5} is sufficient to reduce the cooling/accretion rate by ~ 10 compared to a pure cooling flow in clusters (with $M_{200} \lesssim 7 \times 10^{14} \, M_\odot$). This value is much smaller compared to the ones considered earlier, and is consistent with the jet efficiency and the fact that only a small fraction of gas at 1 kpc is accreted onto the supermassive black hole (SMBH). The feedback efficiency in earlier works was so high that the cluster core reached equilibrium in a hot state without much precipitation, unlike what is observed in cool-core clusters. We find hysteresis cycles in all our simulations with cold mode feedback: *condensation* of cold gas when the ratio of the cooling-time to the free-fall time (t_{cool}/t_{ff}) is $\lesssim 10$ leads to a sudden enhancement in the accretion rate; a large accretion rate causes strong jets and *overheating* of the hot intracluster medium such that $t_{cool}/t_{ff} > 10$; further condensation of cold gas is suppressed and the accretion rate falls, leading to slow cooling of the core and condensation of cold gas, restarting the cycle. Therefore, there is a spread in core properties, such as the jet power, accretion rate, for the same value of core entropy or t_{cool}/t_{ff}. A smaller number of cycles is observed for higher efficiencies and for lower mass halos because the core is overheated to a longer cooling time. The 3D simulations show the formation of a few-kpc scale, rotationally supported, massive ($\sim 10^{11} \, M_\odot$) cold gas torus. Since the torus gas is not accreted onto the SMBH, it is largely decoupled from the feedback cycle. The radially dominant cold gas ($T < 5 \times 10^4$ K; $|v_r| > |v_\phi|$) consists of fast cold gas uplifted by AGN jets and freely infalling cold gas condensing out of the core. The radially dominant cold gas extends out to 25 kpc for the fiducial run (halo mass $7 \times 10^{14} \, M_\odot$ and feedback efficiency 6×10^{-5}), with the average mass inflow rate dominating the outflow rate by a factor of ≈ 2. We compare our simulation results with recent observations.

Key words: galaxies: clusters: intracluster medium – galaxies: halos – galaxies: jets

1. INTRODUCTION

The majority of baryons in galaxy clusters are in the form of a hot plasma known as the intracluster medium (ICM). In the absence of cooling and heating, the ICM is expected to follow self-similar profiles for density, temperature, etc., irrespective of the halo mass (Kaiser 1986, 1991; see also the review by Voit 2005). However, self-similarity is not observed in either groups or clusters (e.g., Balogh et al. 1999; Ponman et al. 1999; Babul et al. 2002). Moreover, the core cooling times in about a third of clusters are shorter than 1 Gyr, much shorter than their age (~Hubble time; e.g., Cavagnolo et al. 2009; Pratt et al. 2009). Thus, we expect cooling to shape the distribution of baryons in these cool-core clusters.

The existence of cool cores with short cooling times in a good fraction of galaxy clusters is a long-standing puzzle. According to the classical cooling flow model, cluster cores with such short cooling times were expected to cool catastrophically and to fuel star formation at a rate of 100–1000 $M_\odot$ yr^{-1} (e.g., Fabian 1994; Lewis et al. 2000). However, cooling, dropout, and star formation at these high rates are never seen in cluster cores (e.g., Edge 2001; Peterson et al. 2003; O'Dea et al. 2008). This means that some source(s) of heating is(are) able to replenish the core cooling losses, thereby preventing runaway cooling and star formation.

While there are potential heat sources, such as the kinetic energy of infalling galaxies and sub-halos (e.g., Dekel & Birnboim 2008), thermal conduction from the hotter outskirts (e.g., Voigt & Fabian 2004; Voit 2011), a *globally stable* mechanism, which increases rapidly with an increasing hot gas density in the core, is required to prevent catastrophic cooling. Observations of several cool-core clusters by *Chandra* and *XMM-Newton* have uncovered active galactic nucleus (AGN)-jet-driven X-ray cavities, whose mechanical power is enough to balance radiative cooling in the core (e.g., Böhringer et al. 2002; Bîrzan et al. 2004; McNamara & Nulsen 2007). The AGN jets are powered by the accretion of the cooling ICM onto the supermassive black hole (SMBH) at the center of the dominant cluster galaxy. Thus, more cooling/accretion leads to an enhanced jet power and ICM heating, closing a feedback loop that prevents runaway cooling in the core.

AGN feedback has been long-suspected to play a role in self-regulating the ICM (e.g., Binney & Tabor 1995; Ciotti & Ostriker 2001; Soker et al. 2001; Babul et al. 2002; McCarthy et al. 2008), but a clear picture has emerged only recently. While AGN feedback should provide feedback heating in cluster cores (as it is enhanced with ICM cooling), it is not obvious if, for reasonable parameters, AGN heating can keep pace with cooling that increases rapidly with an increasing core density. Moreover, the dense core gas is expected to be highly

susceptible to fragmentation, leading to the formation of a multiphase medium consisting of cold dense clouds condensing from the hot diffuse ICM itself. Pizzolato & Soker (2005) suggest that AGN outbursts that result in the heating of the cluster cores are due to the infall and accretion of these cold clumps.

The importance of cold gas precipitation/feedback has also been highlighted by several recent observations. The fact that there is some multiphase-cooling/star formation, albeit at a much smaller rate than predicted by the cooling flow estimate (Soker et al. 2001), ties well with the idea of a small fraction of the thermally unstable core gas cooling to the stable atomic and molecular temperatures. A lot of this cold gas is expected to form stars, but some should be accreted onto the central SMBH. Reservoirs of atomic (e.g., Crawford et al. 1999; McDonald et al. 2011a; Werner et al. 2014) and molecular gas (e.g., Donahue et al. 2000; Edge 2001; Salomé et al. 2006; Russell et al. 2014; O'Sullivan et al. 2015), both extended and centrally concentrated, and ongoing star formation (e.g., Bildfell et al. 2008; Hicks et al. 2010; McDonald et al. 2011b) are observed in a lot of cool-core clusters. Additionally, powerful radio jets/bubbles observed in most cool-core clusters (Cavagnolo et al. 2008; Mittal et al. 2009) can be interpreted as a signature of kinetic feedback due to cold gas accretion onto the SMBH.

Since cool cores are in rough global thermal balance (i.e., the cooling rate minus the heating rate is smaller than just the radiative cooling rate), the existence of cold gas in cluster cores can be understood as a consequence of local thermal instability in a weakly stratified atmosphere (McCourt et al. 2012; Sharma et al. 2012b; Singh & Sharma 2015). The idealized simulations, which impose global thermal equilibrium in the ICM, show that the nonlinear evolution of local thermal instability leads to in situ condensation of cold gas only if the ratio of the cooling time and the freefall time ($t_{\rm cool}/t_{\rm ff}$) is $\lesssim 10$ (Sharma et al. 2012b).

This model has the attractive feature that once the local thermal instability sets in and the cold gas begins to condense out of the dense ICM, it typically falls freely toward the center. Some of the infalling cold gas has sufficiently low angular momentum to be accreted by the SMBH, resulting in the cold phase mass accretion rate onto SMBHs that can exceed the hot/Bondi accretion rate by a factor $\sim$10–100 (Sharma et al. 2012b; Gaspari et al. 2013). This enhanced accretion rate in the cold phase can explain both the global thermal balance in cluster cores and the general lack of massive cooling flows in almost all cool-core clusters whereas, the hot-mode (Bondi) accretion rate appears inadequate by orders of magnitude (e.g., McNamara et al. 2011).

In detail, the precipitation of the cold gas, followed by a sudden increase in the accretion rate onto the SMBHs, leads to an increase in jet/cavity power and (slight) overheating of the core. The core expands and as the ratio $t_{\rm cool}/t_{\rm ff}$ rises above the threshold value of $t_{\rm cool}/t_{\rm ff} = 10$, the gas is no longer prone to condensation. The accretion rate drops, as does the jet power. The core cools slowly and the whole cycle starts again when $t_{\rm cool}/t_{\rm ff} \lesssim 10$. The frequency of heating/cooling cycles depends on jet efficiency and the halo mass. These features of the cold feedback model are verified in our numerical simulations.

In fact, the simple criterion of $t_{\rm cool}/t_{\rm ff} \lesssim 10$ for the onset of local thermal instability is expected to be generic—applicable not only to the ICM but also the intragroup medium (IGrM)

and the circumgalactic medium (CGM) of all galaxies, including the Milky way (Sharma et al. 2012a; Voit et al. 2015b). This, in turn, has far-reaching implications for providing a common framework for understanding the breaking of self-similarity in the properties of hot gas across the hierarchy, from galaxies to groups to clusters, the presence of multi-phase gas in group and clusters cores, and the detection of cold gas in galaxies at distances of $\sim$100 kpc (e.g., Werk et al. 2014). In fact, recent more realistic AGN jet feedback simulations show that cold gas condensation begins when the $t_{\rm cool}/t_{\rm ff} \lesssim 10$ condition is met, and two distinct cold gas structures emerge: extended cold filaments which go out 10s of kpc; and a few-kpc rotationally supported cold torus (Gaspari et al. 2012; Li & Bryan 2014a, 2014b). This dichotomy in cold gas distribution is also seen in observations (e.g., McDonald et al. 2011a).

Now that the theoretical models are satisfactorily able to describe the basic state of the ICM in cool cluster cores, and since observations of cold gas and jets/cavities are rapidly accumulating, it is ripe to make detailed comparisons between observations and numerical simulations. We also aim to investigate the similarities and differences in cold gas and jet/bubble properties as a function of the halo mass and feedback efficiency.

In this paper, we focus on cool-core clusters and have carried out three-dimensional (3D) and two-dimensional (2D; axisymmetric) simulations of the interaction of feedback-driven AGN jets with the ICM over cosmological timescales, varying the halo mass and the feedback efficiency. The 3D simulations, which should correspond more closely to reality, show the formation of a cold, massive, angular-momentum-supported torus, as seen in previous works (Gaspari et al. 2012; Li & Bryan 2014a, 2014b). This massive cold torus is decoupled from the AGN feedback cycle, which is governed by the low angular momentum, radially dominant ($|v_r| > |v_\phi|$, v_r/v_ϕ is the radial/azimuthal component of the velocity) infalling cold gas. Angular-momentum-supported gas is absent in 2D simulations because of axisymmetry and the absence of rotation in the initial state (stochastic angular momentum can be generated in 3D because of $\partial/\partial\phi$ terms in the angular momentum equation). However, 2D simulations are useful for two reasons: first, they show similar behavior to 3D simulations, if we only consider the radially dominant ($|v_r| > |v_\phi|$) cold gas; second, they are much cheaper to run for long timescales, and thus are useful to do parameter scans in halo mass and accretion efficiency.

Compared to previous works (Gaspari et al. 2012; Li & Bryan 2014a, 2014b), we have carried out simulations with smaller feedback jet efficiencies. We find that a feedback efficiency as low as 6×10^{-5} (ratio of the input jet power and $\dot{M}_{\rm acc}c^2$, where $\dot{M}_{\rm acc}$ is the accretion rate measured at 1 kpc) is sufficient to reduce the mass accretion/cooling rate by a factor of about 10 compared to the cooling flow value in groups and clusters. Such a low feedback efficiency fits in nicely with the observations that suggest that only a small fraction ($\sim$0.01) of the available gas is accreted by the SMBH (e.g., Loewenstein et al. 2001), and with the estimate of jet efficiency ($\sim$0.001–0.01) with respect to the SMBH accretion rate (e.g., Benson & Babul 2009). Moreover, jets in SMBHs are observed predominantly when the accretion rate is $\lesssim$0.01 the Eddington value (e.g., Narayan & Yi 1995; Merloni et al. 2003); i.e., $\lesssim$0.22 $M_\odot\,{\rm yr}^{-1}$ for a $10^9\,M_\odot$ SMBH. The expected mass

Table 1
Table of Runs

Label	Dim.	$N_r \times N_\theta \times N_\phi$	Min. Resolution (kpc)	M_{200} ($M_\odot$)	Jet Efficiency (ϵ)	$\langle \dot{M}_{acc} \rangle^b$ ($M_\odot$ yr^{-1})	$\langle \dot{M}_{acc,hot} \rangle / \langle \dot{M}_{acc,cold} \rangle$	Jet Duty Cycle[c] (%)
C6m5D3[a]	3	$256 \times 128 \times 32$	0.02	7×10^{14}	6×10^{-5}	25.1 (244.2)[b]	0.2 (0.06)	59.6
C5m4D3	3	$256 \times 128 \times 32$	0.02	7×10^{14}	5×10^{-4}	7	0.78	82
C1m2-D3	3	$256 \times 128 \times 32$	0.02	7×10^{14}	0.01	1.9	1.3	99.8
C6m5D2[a]	2	$512 \times 256 \times 1$	0.01	7×10^{14}	6×10^{-5}	23.5 (170)	0.23 (0.19)	64.8
C6m6D2	2	$512 \times 256 \times 1$	0.01	7×10^{14}	6×10^{-6}	153	0.27	47.3
C1m2-D2	2	$512 \times 256 \times 1$	0.01	7×10^{14}	0.01	0.77	14.8	99.8
C1m4D2	2	$512 \times 256 \times 1$	0.01	7×10^{14}	10^{-4}	13.7	0.3	63.8
C5m4D2	2	$512 \times 256 \times 1$	0.01	7×10^{14}	5×10^{-4}	5.1	1.6	72.9
M6m6D2	2	$512 \times 256 \times 1$	0.014	1.8×10^{15}	6×10^{-6}	293 (299)	0.3 (0.5)	0.0
M6m5D2	2	$512 \times 256 \times 1$	0.014	1.8×10^{15}	6×10^{-5}	77.7	0.58	50.1
M1m4D2	2	$512 \times 256 \times 1$	0.014	1.8×10^{15}	10^{-4}	48.18	0.62	47.1
M5m4D2	2	$512 \times 256 \times 1$	0.014	1.8×10^{15}	5×10^{-4}	18.7	2.9	63.8
M1m2-D2	2	$512 \times 256 \times 1$	0.014	1.8×10^{15}	0.01	8.1	3.7×10^5	99.8

Notes. "C" in the label stands for a cluster ($M_{200} = 7 \times 10^{14}\ M_\odot$) and "$M$" for a massive cluster ($M_{200} = 1.8 \times 10^{15}\ M_\odot$). Label C6m5D3 indicates that it is a cluster run in 3D with an efficiency $\epsilon = 6 \times 10^{-5}$ (Equation (6)).
[a] The fiducial 3D and 2D runs.
[b] Angular brackets denote time average over the full run. The quantities in brackets denote values for a pure cooling flow ($\dot{M}_{cf}$). Note that eight grid points close to the poles are excluded when calculating the accretion rates.
[c] Jet duty cycle is defined as the fraction of total time for which the jet power is $>10^{40}$ erg s^{-1}.

accretion rate onto the SMBH in our simulations (~ 0.01 times $\dot{M}_{acc}$ in Table 1) satisfies this constraint.

We have analyzed the velocity-radius distribution of the cold gas in our simulations to compare with recent *ALMA* and *Herschel* observations of cold gas structure and kinematics in galaxy/cluster cores (e.g., David et al. 2014; McNamara et al. 2014; Werner et al. 2014). Our simulations help in interpreting observations of cold gas outflows and inflows at scales $\gtrsim 10$ kpc, and the rotationally supported cold torus at scales $\lesssim 5$ kpc. In our simulations, the fast ($\gtrsim 500$ km s^{-1}) atomic/molecular outflows are uplifted by the outgoing AGN jet. The slower ($\lesssim 300$ km s^{-1}) infall of cold gas is due to condensation in the dense core. The cold gas in the rotationally supported torus is at the local circular velocity (~ 200 km s^{-1}).

Our paper is organized as follows. In Section 2 we present the numerical setup, in particular our implementation of mass and kinetic energy injection due to AGN jets. Section 3 presents the key results from our 3D and 2D simulations, a comparison of 3D versus 2D, and the impact of parameters such as feedback efficiency and halo mass on our results. In Section 4 we discuss our results and compare with previous simulations and observations, and we conclude with a brief summary in Section 5.

2. NUMERICAL SETUP AND GOVERNING EQUATIONS

We modify the ZEUS-MP code, a widely used finite-difference MHD code (Hayes et al. 2006), to simulate cooling and AGN feedback cycles in galaxy clusters. We solve the standard hydrodynamic equations using spherical (r, θ, ϕ) coordinates, with cooling, external gravity, and mass and momentum source terms due to AGN feedback:

$$\frac{\partial \rho}{\partial t} + \nabla \cdot (\rho v) = S_\rho, \qquad (1)$$

$$\frac{\partial \rho v}{\partial t} + \nabla \cdot (\rho v \otimes v) = -\nabla p - \rho \nabla \Phi + S_\rho v_{jet} \hat{r}, \qquad (2)$$

$$e \frac{d}{dt} \ln(p / \hat{\rho}^{\hat{\gamma}}) = -n_e n_i \Lambda(T), \qquad (3)$$

where ρ is the mass density, v is the fluid velocity, $p = (\gamma - 1)e$ is the pressure (e is the internal energy density and $\gamma = 5/3$ is the adiabatic index), $\Lambda(T)$ is the temperature-dependent cooling function, n_e (n_i) is the electron (ion) number density given by $\rho / [\mu_{e(i)} m_p]$ ($\mu_e = 1.18$ and $\mu_i = 1.3$ are the mean molecular weights per electron and per ion, respectively, for the ICM with a third solar metallicity). For the cooling function, we use a fit proposed in Sharma et al. (2010) (their Equation (12) and solid line in their Figure 1) with a stable phase at 10^4 K.

In addition to the terms shown in Equations (1)–(3), the code uses the standard explicit artificial viscosity, and has implicit diffusion associated with the numerical scheme (Stone & Norman 1992). In addition to the standard nonlinear viscosity, we use the linear viscosity, as recommended by Hayes et al. (2006) for strong shocks (see their Appendix B3.2).

We use a fixed external Navarro–Frenk–White (NFW) gravitational potential $\Phi(r)$ due to the dark matter halo (Navarro et al. 1996);

$$\Phi(r) = -\frac{GM_{200}}{r} \frac{\ln(1 + c_{200} r / r_{200})}{\left[\ln(1 + c_{200}) - c_{200}/(1 + c_{200}) \right]}, \qquad (4)$$

where M_{200} (r_{200}) is the characteristic halo mass (radius) and $c_{200} \equiv r_{200}/r_s$ is the concentration parameter; the dark matter density within r_{200} is 200 times the critical density of the universe and r_s is the scale radius. In this paper we focus on cluster and massive cluster runs with $M_{200} = 7 \times 10^{14}\ M_\odot$ and

$1.8 \times 10^{15} \, M_{\odot}$, respectively, and adopt $c_{200} = 4.7$ for all models.

We include the source terms S_ρ for mass and $S_\rho v_{\rm jet} \hat{r}$ for the radial momentum to drive AGN jets ($v_{\rm jet}$ is the velocity which the jet matter is put in).[3] These source terms and the cooling term (in Equation (3)) are applied in an operator-split fashion. The mass and momentum source terms are approximated forward in time and centered in space. The cooling term is applied using a semi-implicit method described in Equations (7) of McCourt et al. (2012).

Our simulations do not include physical processes like star formation and supernova feedback. Star formation may deplete some of the cold gas available in the cores (see Li et al. 2015), but this is unlikely to change our results for a realistic model of star formation. Supernova feedback is energetically subdominant compared to AGN feedback, and cannot realistically suppress cluster cooling flows (e.g., Saro et al. 2006). We only include the most relevant physical processes, namely cooling and AGN jet feedback, in our present simulations.

2.1. Jet Implementation

Jets are implemented in the active domain by adding mass and momentum source terms as shown in Equations (1) and (2). The source terms are negligible outside a small biconical region centered at the origin around $\theta = 0, \, \pi$, mimicking mass and momentum injection by fast bipolar AGN jets.

The density source term is implemented as

$$S_\rho(r, \theta) = \mathcal{N} \dot{M}_{\rm jet} \psi(r, \theta),$$

where $\dot{M}_{\rm jet}$ is the *single-jet* mass loading rate,

$$\psi(r, \theta) = \left[2 + \tanh\left(\frac{\theta_{\rm jet} - \theta}{\sigma_\theta} \right) + \tanh\left(\frac{\theta_{\rm jet} + \theta - \pi}{\sigma_\theta} \right) \right]$$
$$\times \left[1 + \tanh\left(\frac{r_{\rm jet} - r}{\sigma_r} \right) \right] \times \frac{1}{4} \tag{5}$$

that describes the spatial distribution of the source term which falls smoothly to zero outside the small biconical jet region of radius $r_{\rm jet}$ and half-opening angle $\theta_{\rm jet}$. We smooth the jet source terms in space because the Kelvin–Helmholtz instability is known to be suppressed due to numerical diffusion in a fast flow if the shear layer is unresolved (e.g., Robertson et al. 2010). The normalization factor

$$\mathcal{N} = \frac{3}{2\pi r_{\rm jet}^3 (1 - \cos \theta_{\rm jet})}$$

ensures that the total mass added due to jets per unit time is $2\dot{M}_{\rm jet}$. All our simulations use the following jet parameters: $\sigma_r = 0.05$ kpc, $\theta_{\rm jet} = \pi/6$, and $\sigma_\theta = 0.05$. The jet source region with an opening angle of $30°$ may sound large but we get similar results with narrower jets. Also, the fast jet extends well beyond the source region and is much narrower (c.f. third panel

---

3 We have also carried out narrow-jet simulations with momentum injection in the vertical [$\hat{z}$] direction, but do not find much difference from our runs with momentum injection in the radial [$\hat{r}$; see Equation (2)] direction.

---

in Figure 1). The jet radius $r_{\rm jet}$ is scaled with the halo mass; i.e.,

$$r_{\rm jet} = 2 \, {\rm kpc} \left(\frac{M_{200}}{7 \times 10^{14} \, M_\odot} \right)^{1/3}.$$

The jet mass-loading rate is calculated from the current mass accretion rate ($\dot{M}_{\rm acc}$) evaluated at the inner radial boundary such that the increase in the jet kinetic energy is a fixed fraction of the energy released via accretion; i.e.,

$$\dot{M}_{\rm jet} v_{\rm jet}^2 = \epsilon \dot{M}_{\rm acc} c^2. \tag{6}$$

We choose the jet velocity $v_{\rm jet} = 3 \times 10^4 \, {\rm km \, s^{-1}}$ (0.1 c; c is the speed of light); such fast velocities are seen in X-ray observations of small-scale outflows in radio galaxies (Tombesi et al. 2010). The jet efficiency (ϵ; our fiducial value is 6×10^{-5}) accounts for both the fraction of the infalling mass at the inner boundary (at 1 kpc for the cluster runs) that is accreted by the SMBH and for the fraction of accretion energy that is channeled into the jet kinetic energy. Our results are insensitive to a reasonable variation in jet parameters ($v_{\rm jet}$, $r_{\rm jet}$, $\theta_{\rm jet}$, σ_r, σ_θ), but depend on the jet efficiency (ϵ).

Like Gaspari et al. (2012), the jet energy is injected only in the form of kinetic energy; we do not add a thermal energy source term corresponding to the jet. We note that Li & Bryan (2014b) have shown that the core evolution does not depend sensitively on the manner in which the feedback energy is partitioned into kinetic or thermal form. Another difference from previous approaches, which use few grid points to inject jet mass/energy, is that our jet injection region is well-resolved.

2.2. Grid, Initial, and Boundary Conditions

Most AGN feedback simulations evolved for cosmological timescales (e.g., Gaspari et al. 2012; Li & Bryan 2014a) use Cartesian grids with mesh refinement. However, we use spherical coordinates with a logarithmically spaced grid in radius, and equal spacing in θ and ϕ. The advantage of a spherical coordinate system is that it gives fine resolution at smaller scales without a complex algorithm. Perhaps more importantly, a spherical setup allows for 2D axisymmetric simulations which are much faster and capture a lot (but not all) of essential physics.

We perform our simulations in spherical coordinates with $0 \leqslant \theta \leqslant \pi$, $0 \leqslant \phi \leqslant 2\pi$, and $r_{\rm min} \leqslant r \leqslant r_{\rm max}$, with

$$r_{\rm [min,max]} = [1, \, 200] \, {\rm kpc} \left(\frac{M_{200}}{7 \times 10^{14} \, M_\odot} \right)^{1/3}.$$

According to self similar scaling, we have scaled all length scales in our simulations (inner/outer radii $r_{\rm min}/r_{\rm max}$, r_{200}, jet radius $r_{\rm jet}$) as $M_{200}^{1/3}$.

We apply outflow boundary conditions (gas is allowed to leave the computational domain but prevented from entering it) at the inner radial boundary. We fix the density and pressure at the outer radial boundary to the initial value and prevent gas from leaving or entering through the outer boundary. Reflective boundary conditions are applied in θ (with the sign of v_ϕ flipped) and periodic boundary conditions are used in ϕ. We noticed that cold gas has a tendency to artificially "stick" at the θ boundaries (mainly in 2D axisymmetric simulations) for our
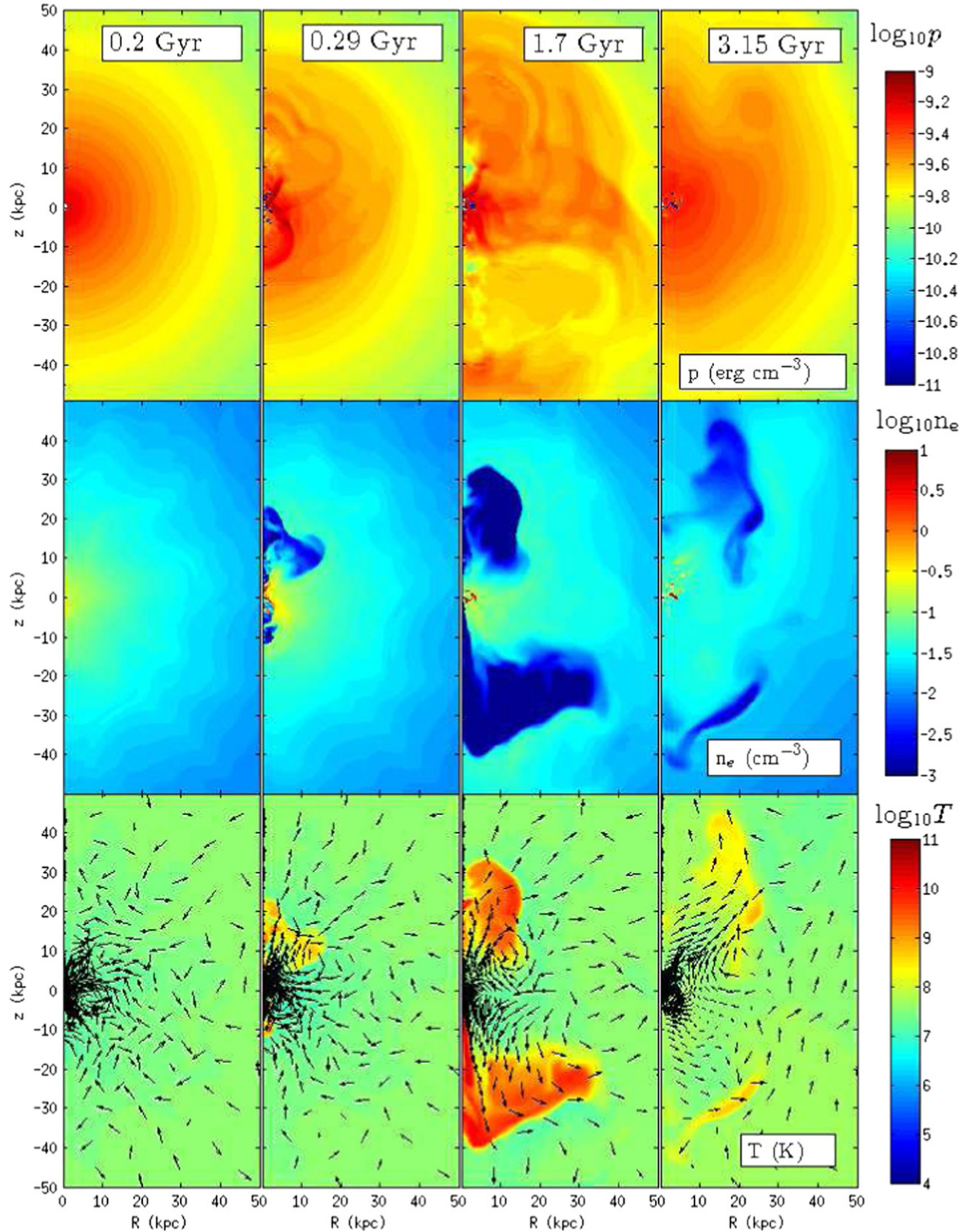
Figure 1. Pressure (upper panel), electron number density (middle panel), and temperature (lower panel) contour plots (R–z plane at $\phi = 0$) in the core at different times for the 3D fiducial run. The density is cutoff at the maximum and the minimum contour level shown. The low-density bubbles/cavities are not symmetric and there are signatures of mixing in the core. The left panel corresponds to a time just before a cooling time in the core. The second panel from the left shows cold gas dredged up by the outgoing jets. The rightmost panel shows infalling extended cold clouds. The pressure maps show the weak outer shock, but the bubbles/cavities so prominent in the density/temperature plot are indiscernible in the pressure map, implying that the bubbles are in pressure equilibrium and buoyant. Also notice the outward-propagating sound waves in the two middle pressure panels in which the jet is active. The infalling/rotationally supported cold gas has a much lower temperature and pressure than the hot phase. The arrows in the temperature plots denote the projected gas velocity unit vectors.

reflective boundary conditions. This cold gas can lead to an unphysically large accretion rate close to the poles, and hence artificially enhanced feedback heating (Equation (6)). Therefore, we exclude 8 grid-points at each pole when calculating the mass accretion rate; these excluded angles correspond to only 0.5% of the total solid angle for 128 grid points in the θ direction. All our diagnostics ($\dot{M}_{\rm acc}$, entropy profiles, etc.) also exclude these small solid angles close to the poles.

The resolution for 3D runs is $256 \times 128 \times 32$ and for 2D runs is 512×256. Since we use a logarithmic grid in the radial direction, the resolution for 256 (512) grid points in the radial direction corresponds to a good resolution of $\Delta r/r = 0.02$ (0.01). The minimum resolution in the radial direction for the fiducial 3D (2D) run is ≈ 0.02 (0.01) kpc. For such a resolution our integrated quantities (mass accretion rate, jet power, cold gas mass, etc.) are converged.

We focus on simulations of a galaxy cluster with $M_{200} = 7 \times 10^{14}\, M_{\odot}$ but with different parameters such as feedback efficiency. For comparison we also carried out simulations for a massive cluster with $M_{200} = 1.8 \times 10^{15}\, M_{\odot}$. The initial conditions are the same as in Sharma et al. (2012b); i.e., we assume the initial entropy profile ($K \equiv T_{\rm keV}/n_e^{2/3}$; $T_{\rm keV}$ is the ICM temperature in keV and n_e is the electron number density) of the form

$$K(r) = K_0 + K_{100}\left(\frac{r}{100\ {\rm kpc}}\right)^{1.4}, \qquad (7)$$

as suggested by Cavagnolo et al. (2009).[4] For our cluster runs, we set $K_0 = 10\ {\rm keV\ cm^2}$ and $K_{100} = 110\ {\rm keV\ cm^2}$ at the start (as in Sharma et al. 2012b). We assume self-similar behavior scaling with M_{200} (Kaiser 1986) to set the initial entropy profile for our massive cluster runs (i.e., we assume $K_0 = 19\ {\rm keV\ cm^2}$ and $K_{100} = 210\ {\rm keV\ cm^2}$; c.f. McCarthy et al. 2008). Except for early transients, our results are independent of the precise choice of the initial values of K_0 and K_{100}.

The outer electron number density is fixed to be $n_e = 0.0015\ {\rm cm^{-3}}$. Given the entropy profile and the density at the outer radius, we can solve for the hydrostatic density and pressure profiles in an NFW potential (Equation (4)). We introduce small (maximum overdensity is 0.3) isobaric density perturbations on top of the smooth density (for details, see Sharma et al. 2012b).

3. RESULTS

In this section we describe the key results from our simulations. Table 1 lists our runs. We begin with the results from our fiducial 3D cluster run (C6m5D3 in Table 1). We show that the one-dimensional (1D) profiles of density, entropy, etc. are consistent with observations. We highlight the cycles of cooling and AGN jet feedback, and the spatial and velocity distribution of the cold gas. We show that there are three components in cold ($T < 5 \times 10^4$ K) gas distribution: a massive, centrally concentrated, rotationally supported torus; spatially extended and fast ($\gtrsim 500\ {\rm km\ s^{-1}}$) outflows correlated with jets; and slower ($\lesssim 300\ {\rm km\ s^{-1}}$) infalling cold gas that condenses out because of local thermal instability. Then we

---

[4] Whether an entropy core exists is debated (Panagoulia et al. 2014), but our results are insensitive to our initial conditions. Our ICM profiles change with time and reach a quasi-steady state which may or may not have an entropy core.

compare the results from our 3D and 2D axisymmetric simulations. We also explore the dependence of our results on the halo mass and the jet efficiency.

3.1. The Fiducial 3D Run

We experimented with different values of jet efficiencies (ϵ; Equation (6)) in our 3D cluster ($M_{200} = 7 \times 10^{14}\, M_{\odot}$) simulations, and found that the average mass accretion rate for $\epsilon = 6 \times 10^{-5}$ was about 10% of a pure cooling flow (see Table 1). Therefore, we choose this as our fiducial value, which is smaller compared to the values chosen by some recent works (Gaspari et al. 2012; Li & Bryan 2014a, 2014b), but is consistent with observational constraints (e.g., O'Dea et al. 2008). Our fiducial value should be considered as the smallest efficiency that is required to prevent a cooling flow in a cluster (this critical efficiency depends on the halo mass, as we shall see later).

The minimum ratio of the cooling time ($t_{\rm cool} \equiv 3nk_B T/[2n_e n_i \Lambda]$) and the local free-fall time ($t_{\rm ff} \equiv [2r/g]^{1/2} = [2r^3/GM(<r)]^{1/2}$) is 7 for the initial ICM; this ratio ($t_{\rm cool}/t_{\rm ff}$) is a good diagnostic of the state of the cluster core in rough thermal balance. Since the initial condition is in hydrostatic equilibrium, there is negligible accretion through the inner boundary, and therefore there is no jet injection. However, after a cooling time in the core (≈ 200 Myr) there is a rise in the accretion rate across the inner boundary ($\dot{M}_{\rm acc}$), and hence in jet momentum injection (Equation (6)). The jet powers a bubble that heats the core and raises $t_{\rm cool}/t_{\rm ff}$, keeping the mass accretion rate well below the cooling flow value (c.f. top panel of Figure 9). After this time the cluster core is in a state of average global thermal balance between radiative cooling and feedback heating via AGN jets.

3.1.1. Jets, Bubbles, and Multiphase Gas

Figures 1 show the snapshots ($r-\theta$ plane at $\phi = 0$) of pressure, density, and temperature at different times for our fiducial 3D run. The X-ray emitting ICM plasma is quite distinct from the dense cold (10^4 K) gas and from the low-density jet/bubble. The cold gas accreting onto SMBH gives rise to AGN jets. Before a cooling time (0.2 Gyr) there are no signs of cooling and jets. After a cooling time, accretion rate through the inner boundary (at 1 kpc) increases and bipolar jets are launched (0.29 Gyr). The jets are not perfectly symmetric, as they are shaped by the presence of cold gas in their way. The inhomogeneities in the ICM enhances mixing with (and stirring of) the ICM core, resulting in effectiveness of our jets even with a low efficiency.

Jets are fast in the injection region but become slow, buoyant, and almost in pressure balance with the ICM (compare the upper and middle panels of Figure 1) because of turbulent drag and sweeping up of the ICM. In absence of further power injection, the bubbles are detached from the jets and rise buoyantly and mix with the ICM at 10s of kpc scales (3.15 Gyr in Figure 1). Most of the cold gas is very centrally concentrated (within 10 kpc), but does condense out at larger radii, although never beyond 30 kpc.

As jets plow through the dense cold gas clouds, forward shock moves ahead of these clouds after partially disrupting them. The collision results in a reverse shock and a huge back-flow of hot jet material that mixes with the cooler ICM, driving
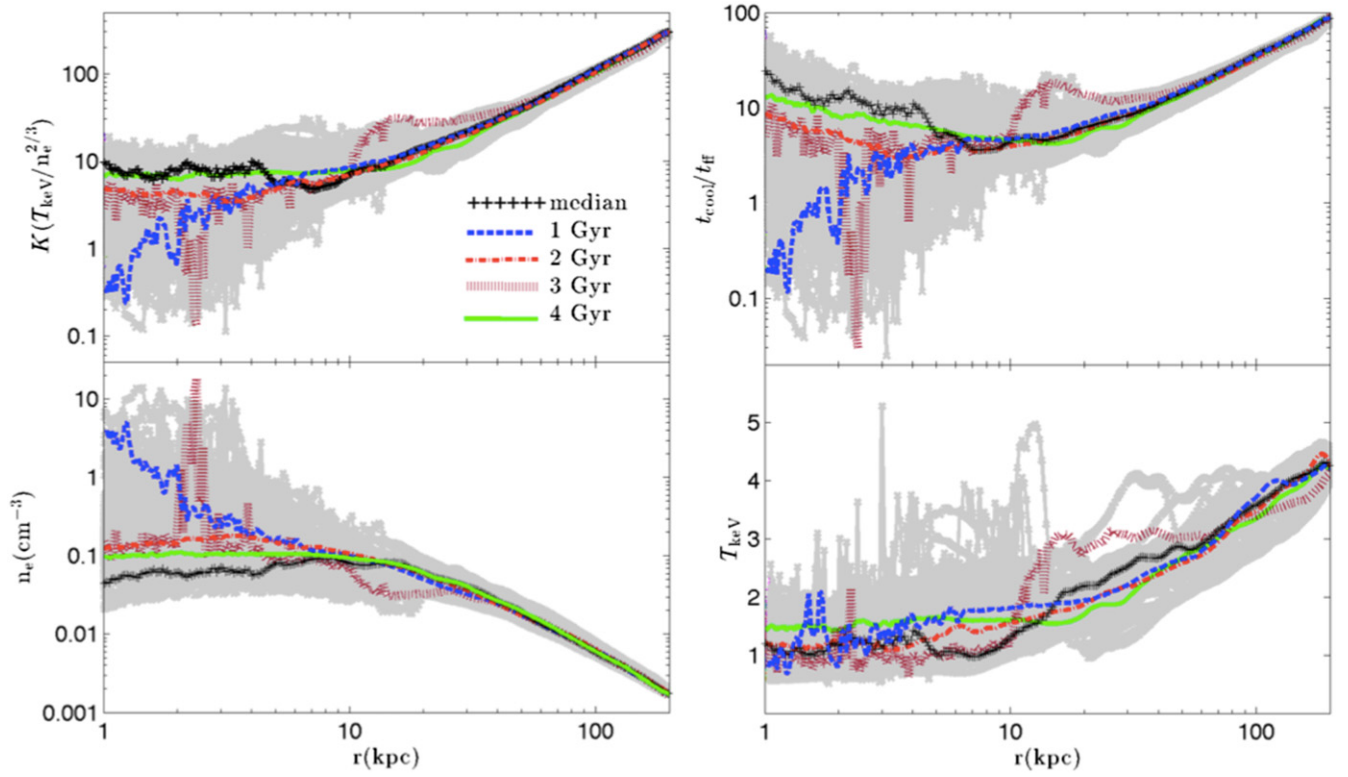
Figure 2. X-ray emissivity-weighted (considering only 0.5–8 keV gas) 1D profiles of important thermodynamic variables as a function of radius. Snapshots at 1–4 Gyr are shown. Various quantities are obtained by combining 1D profiles of density and pressure. The median and standard deviation (σ) of entropy ($K \equiv T_{\rm keV}/n_e^{2/3}$) at 20 kpc are calculated. Various profiles corresponding to the median entropy at 20 kpc (14 keV cm^2) are shown in different panels (black lines with "+"). Thick gray lines show the profiles for which the entropy at 20 kpc is within $1 - \sigma$ of its median value.

the core entropy to higher values. These back-flows and mixing are mainly responsible for heating the cluster core.

3.1.2. Radial Profiles

Before discussing the detailed kinematics of cold gas and jet cycles, we show in Figure 2 the 1D profiles of important thermodynamic quantities (entropy $[T_{\rm keV}/n_e^{2/3}]$, $t_{\rm cool}/t_{\rm ff}$, n_e, $T_{\rm keV}$) as a function of radius for the fiducial 3D run. In addition to the instantaneous profiles (at 1–4 Gyr), the median profile and spread about it are shown. The median is calculated for the entropy measured at 20 kpc (roughly the core size) and all the profiles with entropy within one standard deviation at the same radius are shown in gray.

The spread in quantities outside $\sim$20 kpc is quite small, but increases toward the center because multiphase cooling (leading to density spikes) and strong jet feedback (leading to overheating) are most effective within the core. The density at 1 Gyr is peaked toward the center, indicating that the cluster core is in a cooling phase. The spikes in density at 3 Gyr have corresponding spikes in entropy and $t_{\rm cool}/t_{\rm ff}$ profiles, but not as prominent in the temperature profile. The temperature fluctuations are rather modest compared to fluctuations in other quantities because of dropout and adiabatic cooling. Temperature profiles show a general increase with radius, as seen in observations.

There is a large spread in entropy toward lower values about the median at radii $<$10 kpc (top left panel in Figure 2). This is because there are short-lived cooling events during which the entropy in the core decreases significantly (simultaneously, density increases and $t_{\rm cool}/t_{\rm ff}$ decreases). On the other hand, the

increase in the core entropy is smaller but lasts for a cooling time, which is longer in this state. This behavior is generic, fairly insensitive to parameters such as the feedback efficiency and the halo mass.

3.1.3. The Cold Torus

While Figure 1 shows that cold gas can be dredged up by AGN jets (second panel; see also Revaz et al. 2008; Pope et al. 2010) and can also condense out of the ICM at large scales (fourth panel), majority of cold gas is at very small scales ($<$5 kpc) in the form of an angular-momentum supported cold torus. Figure 3 shows the zoomed-in density snapshots in the equatorial ($\theta = \pi/2$) plane at different times; the arrows show the projection of velocity unit vectors. As the cluster evolves the cold gas, condensing out of the hot ICM, gains angular momentum from jet-driven turbulence. Because of a significant angular velocity, an angular momentum barrier forms and cold gas circularizes at small radii.

Unlike Li & Bryan (2014b), our cold torus is dynamic in nature as AGN jets disrupt it time and again, but it reforms due to cooling. Figure 3 shows the evolution of the torus at various stages of the simulation. The top left panel of Figure 3 shows the cluster center at 0.5 Gyr. Small cold gas clouds are accumulating in the core after the first active AGN phase. At 1.3 Gyr, cold gas accreting through the inner boundary has an anti-clockwise rotational sense. At 1.98 Gyr, cold gas (and the hot gas out of which it condenses) is rotating clockwise. Jet activity leading up to this phase has reversed the azimuthal velocity of the cold gas. At all times after this the dynamic cold gas torus rotates in a clockwise sense, essentially because the
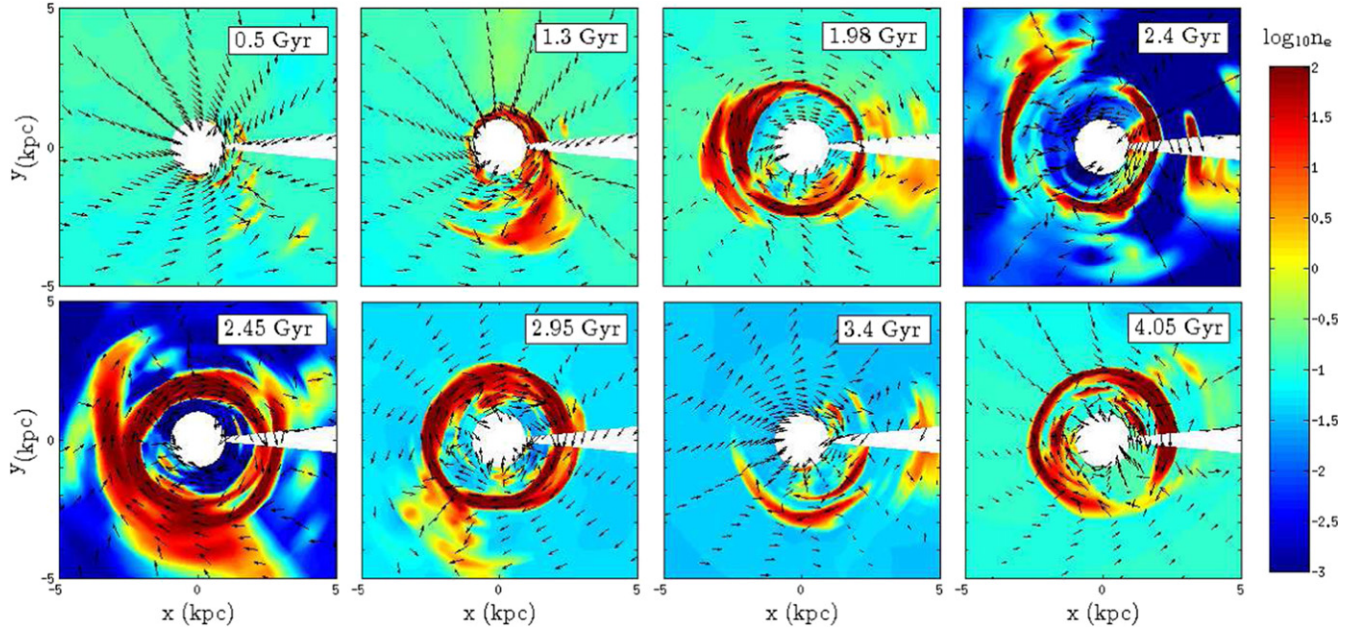
Figure 3. 2D ($z = 0$) contour plots of electron number density (in cm^{-3}) in the mid-plane of the very inner region at different times for the fiducial 3D run, with the projection of the velocity unit-vector represented by arrows. The top left panel shows the beginning of the infall of cold gas with random angular momentum. The second top left panel shows an anti-clockwise transient torus. All times after this show a clockwise torus in the mid-plane that waxes and wanes because of cooling and AGN heating cycles. Even at late times the cold torus is not stable and gets disrupted by jets.

mass (and angular momentum) in the rotating torus is much larger than the newly condensing cold gas.

The torus gets disrupted due to jet activity but forms again quickly. The snapshots at 2.4 and 2.45 Gyr show that the inner region is covered by the very hot/dilute jet material. If the jets were rapidly changing direction as argued by Babul et al. (2013), we would in fact expect the cold gas torus to be occasionally disrupted by the jets. In the present simulations, however, this behavior is an artifact of our feedback prescription; we scale the jet power with the instantaneous mass inflow rate through the inner boundary (see Equation (6)). Even small oscillations of the cold torus can sometimes lead to a large instantaneous mass inflow through the inner boundary and hence an explosive jet event. The reassuring fact is that these explosive "events" are rare and the jet material is quickly mixed with the ICM after these. In reality, most of the cold gas in the torus will be consumed by star formation. Only the low angular momentum cold gas that circularizes closer in ($\lesssim 100$ pc) can be accreted by the SMBH at a short enough timescale.

A cold torus forms in all our 3D cluster simulations with different efficiencies. However, extended cold gas is lacking at late times in simulations with high jet efficiencies. Li & Bryan (2014b) show that after 3 Gyr the cold gas settles down in form of a stable torus, with no further condensation of extended cold gas. This is inconsistent with observations which show that about a third of cool-core clusters show Hα filaments extending out to 10s of kpc from the center (McDonald et al. 2010). The bottom panels in Figure 3 from our fiducial run show that the torus is unsteady even at late times with extended cold gas condensing out till the end of our run. We compare our results in detail with Li & Bryan (2014b) in Section 4.1.

3.1.4. Velocity and Space Distribution of Cold Gas

We find it very instructive to classify the cold gas into two components: most of the mass is in the *rotationally dominant* gas at $\lesssim 5$ kpc; a smaller fraction is in a *radially dominant* component spread over 20 kpc. Figure 4 shows the velocity and space distribution of rotationally (the left two panels; $d^2 M/d \ln|v_\phi| dr$ and $d^2 M/d \ln|v_r| dr$; $|v_\phi| > |v_r|$) and radially (the right two panels; $d^2 M/d \ln|v_\phi| dr$ and $d^2 M/d \ln|v_r| dr$; $|v_\phi| < |v_r|$) dominant cold ($T < 5 \times 10^4$ K) gas, averaged from 1 to 4 Gyr. The rotationally dominant gas distribution ($|v_\phi| > |v_r|$; two left panels in Figure 4) shows two peaks at $v_\phi \approx \pm 150$–200 km s^{-1} and $r \approx 1.5$–4 kpc, corresponding to the cold tori seen in Figure 3. The radial velocity is $\lesssim 100$ km s^{-1}.

The distribution of the radially dominant cold gas in Figure 4 is quite different from the rotationally dominant gas. In addition to a larger radial extent, the radial velocity of the radially dominant component is much larger, going up to ± 600 km s^{-1}, much larger than the maximum azimuthal speed. The radial velocity of the closer in gas ($\lesssim 5$ kpc) is even larger for the outflowing ($v_r > 0$) component because it is dredged up by the fast jet material; tiny mass in the cold gas is seen to reach a velocity close to $v_{jet} = 0.1c$. The mass in the infalling radially dominant cold gas is $\approx$ twice that of the outgoing cold gas.

Figure 5 shows the 1D velocity distribution of the cold gas averaged from 1 to 4 Gyr. The two large, sharp peaks correspond to the massive clockwise rotating cold torus. The radially dominant component ($|v_r| > |v_\phi|$) shows a prominent high velocity tail in the positive direction. The negative velocity component for velocities larger than 300 km s^{-1} is also dominated by the radially infalling (rather than rotationally dominant) gas, sometimes affected by the fast jet back-flows. The maximum velocity peak of the radially and rotationally dominant cold gas coincide at ≈ 150–200 km s^{-1}, corresponding to the circular velocity at ~ 5 kpc.
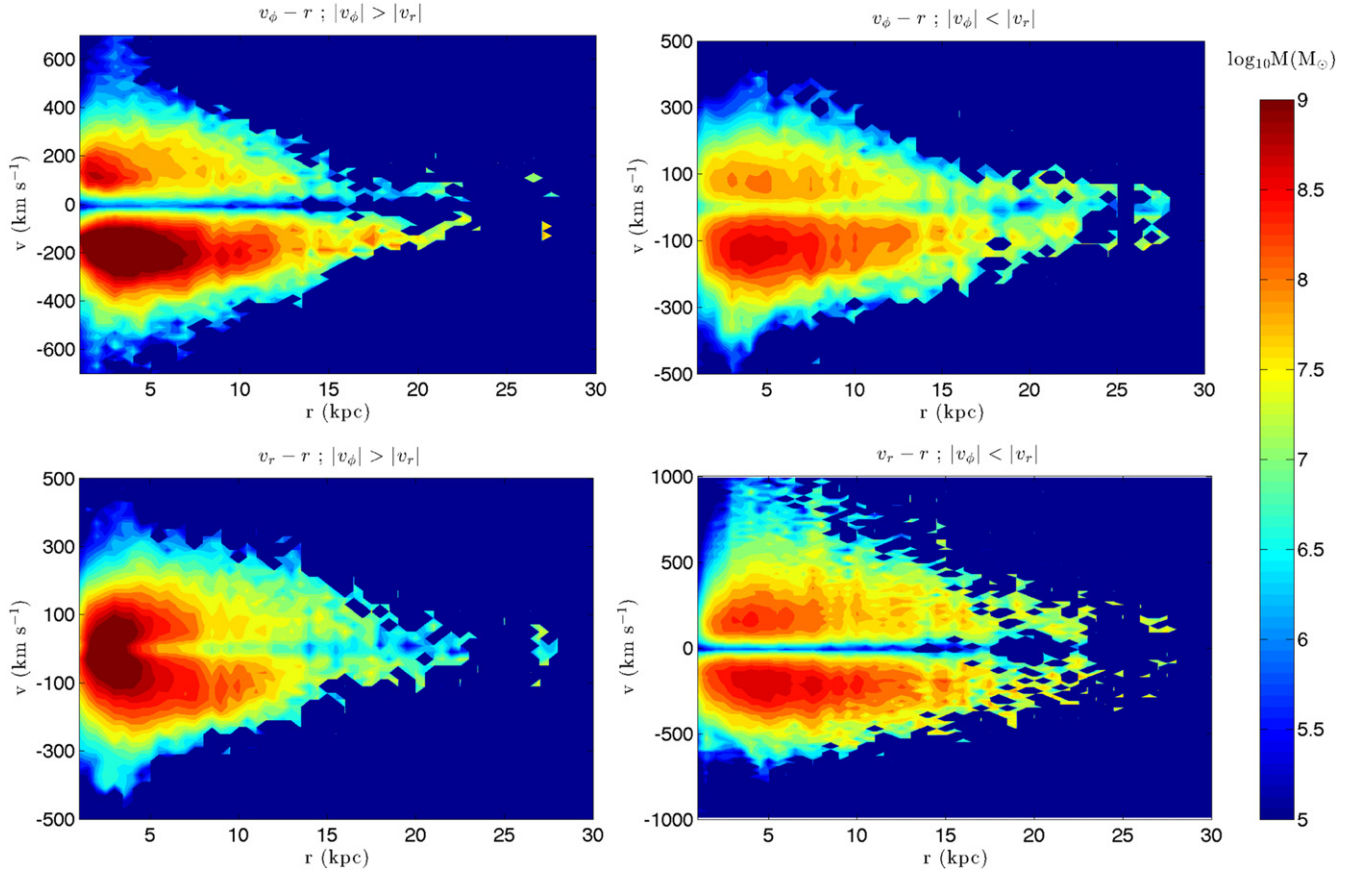
Figure 4. Velocity-radius distribution of the cold gas ($T < 5 \times 10^4$ K) mass averaged from 1 to 4 Gyr. The top left panel shows the $v_\phi - r$ mass distribution ($\frac{d^2 M}{d \ln |v_\phi| \, d \ln r}$; $\Delta v_\phi = \Delta v_r = 20$ km s^{-1}, $\Delta r = 0.5$ kpc are the bin-sizes) for the rotationally dominant ($|v_\phi| > |v_r|$) gas and the bottom left panel shows the $v_r - r$ distribution for the same gas. The top right panel shows the $v_\phi - r$ distribution for the radially dominant ($|v_r| > |v_\phi|$) cold gas and the bottom right panel shows the $v_r - r \left(\frac{d^2 M}{d \ln |v_r| \, d \ln r} \right)$ distribution for the same gas. Some of the salient features are: the rotationally dominant cold gas, which is concentrated mainly within 5 kpc, is more abundant by a factor ~40 than the radially dominant gas; the dominant rotationally supported clockwise cold torus with a negligible radial velocity (see Figure 3) is clearly visible in the two left panels; the radially dominant cold gas (with $|v_r| > |v_\phi|$) is much more radially extended, going out to 25 kpc; the bottom right panel shows that the infalling ($v_r < 0$) cold gas dominates over the outgoing cold gas (by a factor ≈2) and that the outgoing cold gas at ≲5 kpc extends to very large velocities.

Figure 6 shows the relationship of infalling and outgoing cold gas at small scales (5 kpc) and AGN jet activity. The cold outflow rate shows large spikes coincident with a sudden rise in AGN jet power, implying that cold gas observed with large velocity (inf Figures 4 and 5) is dredged up by fast moving jets. The coincidence is particularly strong when a massive cold gas torus is present at small scales. For steady cooling in absence of angular momentum, we expect the mass inflow rate at 5 kpc and 1 kpc to closely follow each other. This is, however, not the case (especially around 2 Gyr) when the majority of infalling cold gas crossing 5 kpc is incorporated in the rotating cold torus, instead of accreting through 1 kpc. Also note that the outflowing cold gas is in form of very short-lived massive spikes, but the inflowing cold gas is smoother. The interpretation is that the outflowing cold gas is associated with the AGN-uplifted cold torus gas, and the infalling cold gas is because of local thermal instability in a gravitational field.

3.1.5. Cooling and Heating Cycles

One of the distinct features of the cold feedback paradigm is that we expect correlations in jet power, cold gas mass, mass accretion rate, min(t_{cool}/t_{ff}), core entropy, etc. The observations

indeed show such correlations (e.g., Figures 1 and 2 in Cavagnolo et al. 2008; see also Sun 2009; McDonald et al. 2011a; Voit et al. 2015). In Figure 7 we make "phase-space" plots of jet power and cold-gas mass (total and the radially dominant component) as a function of min(t_{cool}/t_{ff}) for our fiducial 3D run.

Evaluating min(t_{cool}/t_{ff}): the ratio t_{cool}/t_{ff} is calculated by making radial profiles of emissivity-weighted (only including plasma in the range of 0.5–8 keV) internal energy and mass densities. They are combined to calculate $t_{cool} \equiv (3/2)nk_B T/(n_e n_i \Lambda)$, and t_{cool}/t_{ff} is calculated by taking its ratio with the free-fall time based on the NFW potential (Equation (4); $t_{ff} \equiv [2r/g]^{1/2}$ where $g \equiv d\Phi/dr$). The broad local minimum in t_{cool}/t_{ff} profile is searched going in from the outer radius and is used as min(t_{cool}/t_{ff}).

Evaluating jet power: the jet power is also calculated in a novel way, which is close to what is done in observations.[5] We consider the grids with mass density lower than a threshold

---

[5] Observers calculate the bubble/cavity mechanical power by assuming it to be in pressure balance with the background ICM and by using a size and an age estimate for the bubble (e.g., see Bîrzan et al. 2004). Indeed, our bubbles are in pressure balance with the ICM, as seen in Figure 1.
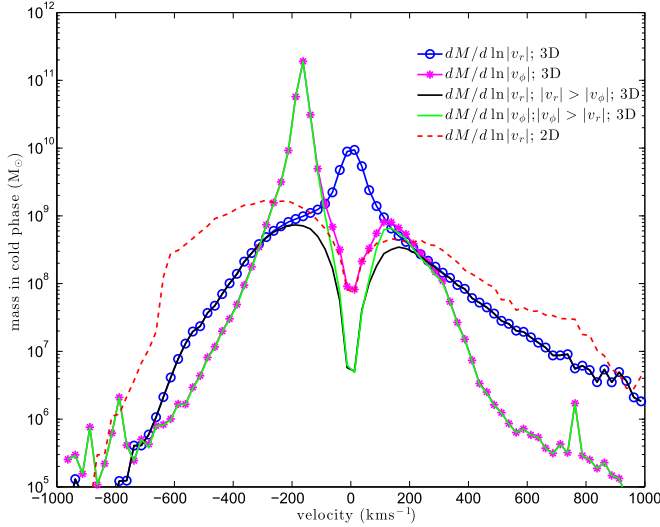
Figure 5. Velocity distribution of cold gas for the 3D fiducial run with respect to the radial and azimuthal velocities. Also shown are the rotationally ($|v_\phi| > |v_r|$) and radially ($|v_r| > |v_\phi|$) dominant components. At large velocities the total and radially/rotationally dominant components coincide but at small velocities they do not, as expected (at low velocities the other component of velocity dominates the mass budget). Also shown (dashed line) is the radial velocity distribution for the 2D fiducial run; the azimuthal velocity is zero for 2D axisymmetric runs.
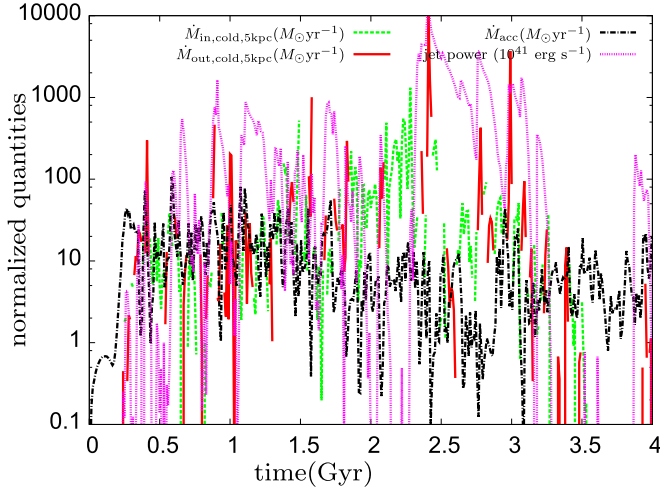
Figure 6. Mass inflow (green short-dashed line) and outflow (red solid line) rates in the cold phase measured at 5 kpc as a function of time. Also shown are the jet power (normalized to 10^{41} erg s^{-1}; how jet power is calculated is described in Section 3.1.5) and the mass accretion rate at 1 kpc (Equation (6)). Note that the largest spikes in the cold outflow rates are mostly associated with a sudden rise in jet energy, indicating cold gas uplifted by jets. The difference between the mass inflow rate at 5 kpc and at 1 kpc (clearly noticeable at ~2 Gyr) leads to the build-up of the rotating cold torus (see Figure 3). Also note that extended cold gas and jets are absent at ~3.75 Gyr.

value (chosen to be 0.17 times the initial minimum density in the computational volume; results are insensitive to the exact value of the threshold density) to belong to the jet/bubble material, and we simply volume-integrate the internal energy density of all such cells to calculate the jet energy (only considering thermal energy; we use $\gamma = 5/3$ for the jet material because it is a non-relativistic hot gas in our simulations; in reality, relativistic particles with $\gamma = 4/3$ are a major component of jets). This density-based definition of the jet material coincides with the visual appearance of the jet. The

jet energy is divided by an estimate of the bubble lifetime (chosen to be 30 Myr, of the order of the dynamical/buoyancy time at 10 kpc; see Table 3 in Bîrzan et al. 2004) to arrive at the jet power. For simplicity, we use the same value of the bubble lifetime at all times in all our runs. A trivial definition of jet power, in which it is proportional to the instantaneous accretion rate at 1 kpc, is given by Equation (6) as $3.4 \times 10^{42} \dot{M}_{acc} (M_\odot \text{ yr}^{-1})$ erg s^{-1}. Assuming this conversion, Figure 6 shows that the two estimates of jet power are comparable in magnitude but vary rather differently with time. This is because while $\dot{M}_{acc}$ is an instantaneous quantity varying on a dynamical timescale, our jet power is based on the jet thermal energy, which is an integrated quantity.

We anticipate cycles in the evolution of min(t_{cool}/t_{ff}) and jet power or the radially dominant cold gas. Imagine that there is no accreting cold gas at the center; in this state without heating the core is expected to cool below $t_{cool}/t_{ff} \sim 10$ (because the accretion rate in the hot mode is small). The $t_{cool}/t_{ff} \lesssim 10$ state is prone to cold-gas condensation and enhanced feedback heating if ϵ is sufficiently high. Energy injection leads to overheating of the core and an increase in t_{cool}/t_{ff}; since condensation/accretion is suppressed in this state, both jet power (because of adiabatic/drag losses) and radially dominant cold gas mass are reduced in this state of $t_{cool}/t_{ff} > 10$. Eventually the core cools again and the cycle starts afresh.

The left panel of Figure 7 shows one of the many jet cycles in our fiducial 3D cluster run. On average jet power versus min(t_{cool}/t_{ff}) evolves in the form of clockwise cycles of various widths (a measure of the range of min[t_{cool}/t_{ff}] before and after the jet event) and heights (jet power). Generally, a smaller t_{cool}/t_{ff} leads to a larger mass accretion rate and a larger jet energy, and therefore larger overheating and a larger min(t_{cool}/t_{ff}). Since the efficiency of our fiducial run is rather small ($\epsilon = 6 \times 10^{-5}$), the cluster core remains with $t_{cool}/t_{ff} < 20$ at most times. In Section 3.2.2 we discuss the dependence of our results on jet efficiency (ϵ).

The middle panel of Figure 7 shows the total mass in cold gas (most of which is in the cold rotating torus) as a function of min(t_{cool}/t_{ff}). We see the mass in the cold torus building up in time. We can easily see that the *total* cold gas mass simply builds up in time (see the green dashed line in the upper panel of Figure 9), and is uncorrelated with min(t_{cool}/t_{ff}). The right panel of Figure 7 shows the mass in the radially dominant cold gas (with $|v_r| > |v_\phi|$) as a function of min(t_{cool}/t_{ff}). This panel also shows a clockwise cycle like the jet power shown in the left panel. A larger radially dominant cold gas mass generally implies a higher accretion rate and a larger jet power, but the features in jet and cold gas cycle are not always varying in an identical fashion. While the global evolution in phase space is clockwise, there is haphazard evolution at smaller timescales (e.g., between 2.5 and 2.9 Gyr).

3.2. The 2D Runs

The 3D simulations are very expensive compared to the 2D ones, not only because the number of grid cells is larger but also because the CFL time step is much smaller. The CFL time step in 3D is dominated by cells close to the polar regions ($\theta = 0, \pi$) and $\propto r \sin\theta \Delta\phi \approx r\Delta\theta\Delta\phi/2$, much smaller than in 2D ($\propto r\Delta\theta$). Our $256 \times 128 \times 32$ (3D) runs have 8 times more grid cells compared to our 512×256 (2D) runs and the CFL time step is ≈0.2 times smaller, making our 3D runs 40 times more expensive than the 2D ones. Therefore, for scans in

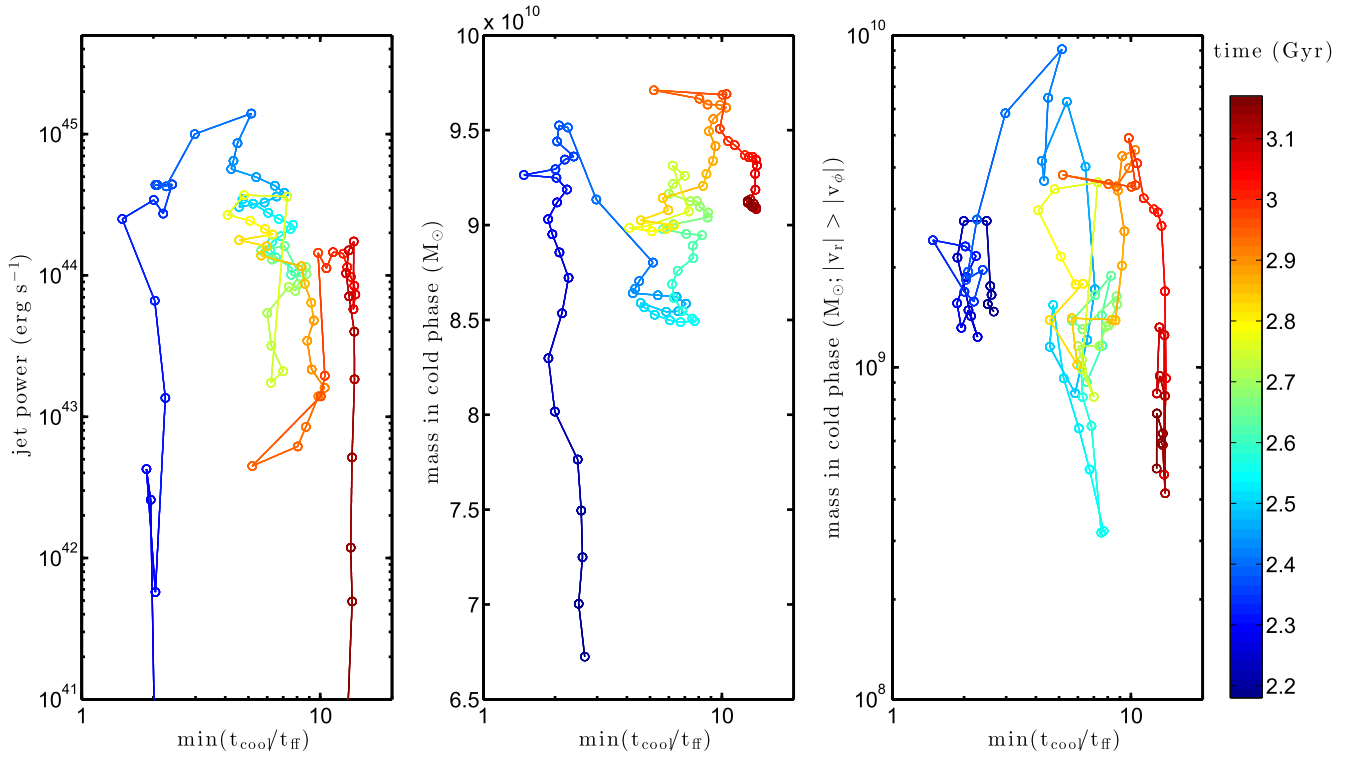**Figure 7.** Variation of jet power, total cold gas mass, and the radially dominant cold gas mass as a function of $\min(t_{\rm cool}/t_{\rm ff})$ for the fiducial 3D run from 2.2 to 3.2 Gyr. Color shows the evolution of cluster in time. While jet power (left panel) and radially dominant cold gas mass (right panel) show clockwise cycles with $\min(t_{\rm cool}/t_{\rm ff})$, the total cold gas mass (middle panel) simply builds up in time. Notice the linear scale for the total cold gas mass instead of a log scale for the other two cases.

various parameters (halo mass, jet efficiency, etc.), only 2D axisymmetric simulations are practical. However, the key drawback is that the initially non-rotating gas cannot gain angular momentum in axisymmetry, and thus 2D simulations do not show the formation of a rotationally supported torus. But, as we discuss shortly, the suppression of cooling flow, nature of radially dominant cold gas, etc. are very similar in 2D and 3D.

In this section we describe different variations on the fiducial setup for our 2D simulations. Section 3.2.1 compares the results from 2D and 3D simulations with cooling and AGN feedback. Section 3.2.2 studies the effect of jet feedback efficiency and the halo mass on the properties of jets and cold gas.

3.2.1. Comparison with 3D

Since 3D simulations are substantially more time consuming compared to the 2D axisymmetric ones, it will be very useful if some robust inferences can be drawn from these faster 2D computations. To compare the 3D simulations with their 2D counterparts, we have carried out the fiducial 3D simulation in 2D with identical parameters (the initial density perturbations in 2D runs are the same as the perturbation for the $\phi = 0$ plane in 3D).

Figure 5 compares the time-averaged velocity distribution of cold gas in 2D and 3D simulations. Since the azimuthal velocity vanishes in 2D axisymmetric simulations, we compare the radial velocity distribution of cold gas in 2D simulations with the radially dominant ($|v_r| > |v_\phi|$) component in 3D. While the outflowing cold gas has a similar distribution in 2D and 3D, the inflowing gas is more dominant in 2D relative to
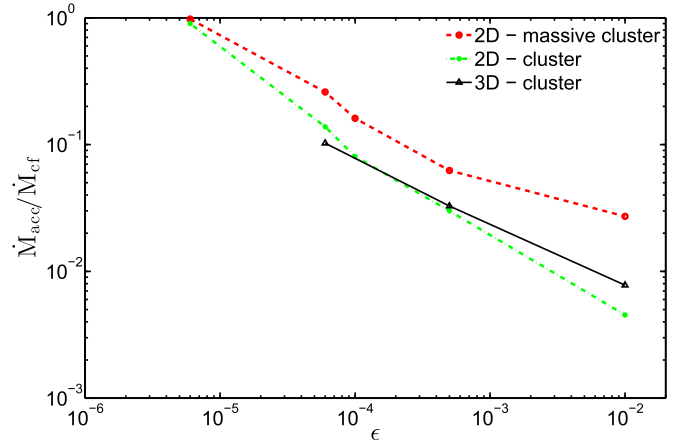

Figure 8. Mass accretion rate relative to the cooling flow value as a function of jet efficiency (Equation (6)) for cluster and massive cluster runs (both 2D and 3D). The accretion rate is suppressed more for a lower halo mass at a fixed ϵ.

3D because in 3D a lot of this infalling cold gas slows down and becomes a part of the rotating cold torus.

Table 1 shows that the mass accretion rate through the inner boundary for the fiducial runs in 2D and 3D are comparable. Unlike in 3D, we note that there is substantial cold gas sticking to the poles in 2D due to numerical reasons. Similarly, in 3D there is a physical accumulation of cold gas in form of a rotating torus.

Figure 8 shows the average mass accretion rate through the inner radius of our simulation volume ($\dot{M}_{\rm acc}$) relative to the cooling flow rate ($\dot{M}_{\rm cf}$). The suppression factor ($\dot{M}_{\rm acc}/\dot{M}_{\rm cf}$) for
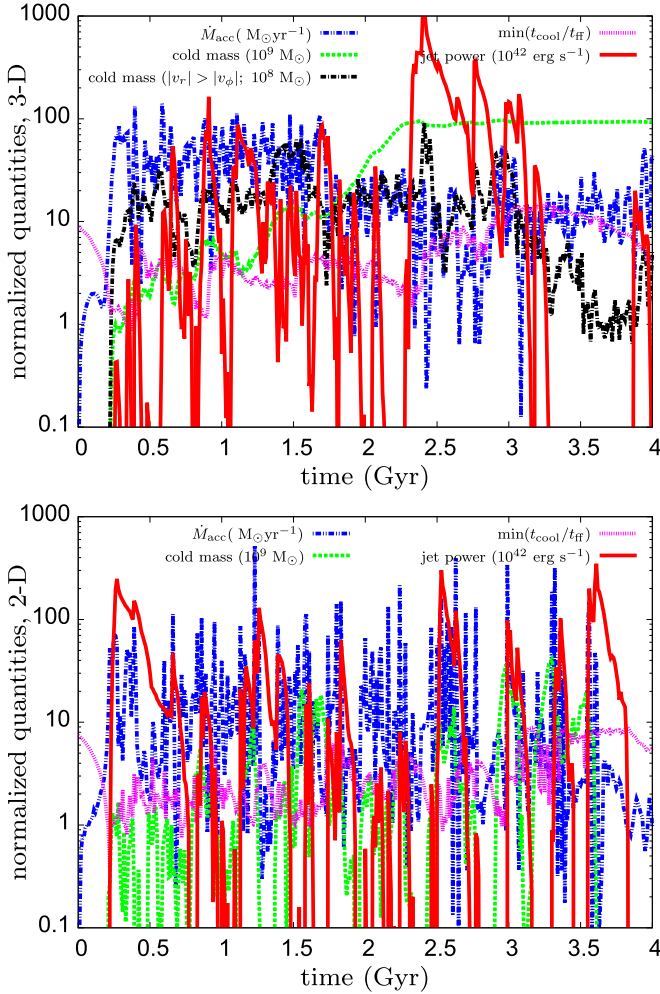
Figure 9. Various quantities (jet power, cold gas mass, radially dominant cold gas mass, min[$t_{\rm cool}/t_{\rm ff}$], $\dot{M}_{\rm acc}$) as a function of time in the fiducial 3D (top panel) and 2D (bottom panel) cluster simulations. The data are sampled every 10 Myr. The cycle shown in Figure 7 are based on the top panel. All quantities, except total cold gas mass, are statistically similar in 3D and 2D. The total cold gas mass, which is dominated by the cold torus, is much larger in 3D and builds up in time. However, the radially dominant cold gas ($|v_r| > |v_\phi|$) mass in 3D is similar to the total cold gas mass in 2D.

3D cluster simulations (with $\epsilon = 6 \times 10^{-5}$, 5×10^{-4}, 0.01) is comparable to 2D.

Figure 9 shows various important quantities, such as jet power, cold gas mass, and mass accretion rate through the inner boundary, as a function of time for the fiducial 3D (upper panel) and 2D (bottom panel) runs. Encouragingly, various quantities, except the total cold gas mass, show similar trends with time in 2D and 3D. The total cold gas mass is much larger in 3D because of the formation of a massive cold torus which is absent in axisymmetry.

In both 2D and 3D runs min($t_{\rm cool}/t_{\rm ff}$) varies in the range 1 to 10, and is roughly anti-correlated with $\dot{M}_{\rm acc}$ and jet power. The maximum jet power goes up to $\sim 10^{45}$ erg s^{-1} in both cases. The mass accretion rate and hence feedback power injection (Equation (6)) is more spiky in 2D (can go above 100 $M_\odot$ yr^{-1} for some times) because, unlike in 3D, the cold gas that is accreted in 2D covers full angle 2π in ϕ because of axisymmetry. The jet power, which is calculated by measuring the instantaneous jet thermal energy, depends on the average mass accretion rate over $\lesssim 100$ Myr rather than the

instantaneous value. Another difference between 2D and 3D is that cold gas can be totally removed (through the inner boundary) after strong feedback jet events in 2D but this never happens in 3D; cold gas (even the radially dominant component) is present at all times because it is very difficult to evaporate/accrete the massive rotating cold torus. There definitely is a depletion in the amount of radially dominant cold gas after a strong feedback event in 3D (at ~ 3.5 Gyr in the top panel of Figure 9).

Although we have not explicitly shown jet power and cold gas "phase-space" plots for our 2D fiducial run, we have verified that it shows cycles similar to the 3D run (left and right panels of Figure 7). Indeed, Figure 9 indicates that the 2D runs should also show clock-wise cycles in jet energy and cold gas mass as a function of min($t_{\rm cool}/t_{\rm ff}$). These cycles just reflect the sudden rise in the accretion rate ($\dot{M}_{\rm acc}$) and jet power due to cold gas condensation and slow relaxation to equilibrium after overheating (notice the fast rise and slow decline in jet energy for individual jet events in both panels of Figure 9).

3.2.2. Dependence on Jet Efficiency and Halo Mass

Till now we have discussed the fiducial cluster simulation with a small feedback efficiency $\epsilon = 6 \times 10^{-5}$. In this section we study the influence of jet efficiency (ϵ) and halo mass (M_{200}) on various properties of the cluster core. Overall, we find that the effect of an increasing halo mass is similar to that of a decreasing feedback efficiency. We compare the efficiencies (ϵ) ranging from 6×10^{-6} to 0.01. We consider two halo masses: a cluster with $M_{200} = 7 \times 10^{14} M_\odot$ and a massive cluster with $M_{200} = 1.8 \times 10^{15} M_\odot$.

Table 1 and Figure 8 show that the feedback efficiency of $\epsilon = 6 \times 10^{-5}$ is able to suppress the cooling flow by about a factor of 10 for a cluster but only by a factor of 4 for a massive cluster. This implies that a larger efficiency is required to suppress a cooling flow in a more massive halo. We note that the pure cooling flow accretion rate decreases with a decreasing halo mass because of a smaller amount of gas in lower mass halos (see the values enclosed in brackets in Table 1).

Figure 8 shows that the suppression factor ($\dot{M}_{\rm acc}/\dot{M}_{\rm cf}$) is smaller for the massive cluster, and scales as $\epsilon^{-2/3}$ for both cluster and massive cluster runs (see also Table 1). A decrease in the accretion rate with an increasing ϵ is not a surprise; a higher feedback efficiency heats the core more and maintains $t_{\rm cool}/t_{\rm ff} \gtrsim 10$ at most times, resulting in only a few cooling/feedback events. While the average jet power ($\sim \epsilon \dot{M}_{\rm acc} c^2 \propto \epsilon^{1/3}$) increases with an increasing ϵ, the core X-ray luminosity decreases. This implies that feedback heating and cooling do not balance each other at all times. Heating dominates cooling just after jet outbursts and cooling dominates in absence of infalling cold gas when $t_{\rm cool}/t_{\rm ff}$ slowly decreases from a value $\gtrsim 10$. Thus, for a larger ϵ, for which a cluster spends more time in a hot/dilute state, the X-ray emission from the core is expected to be smaller (c.f., Figure 12).

Figure 10 shows the mass accretion rate (averaged over 50 Myr bins) as a function of time for our 2D cluster and massive cluster runs with different feedback efficiencies. The solid red line corresponds to the fiducial 2D cluster run (with $\epsilon = 6 \times 10^{-5}$). The green dotted line with a marker, which corresponds to a ten times lower efficiency ($\epsilon = 6 \times 10^{-6}$), shows an accretion rate comparable to a cooling flow at most times (see also Table 1). The cluster run with 10 times higher
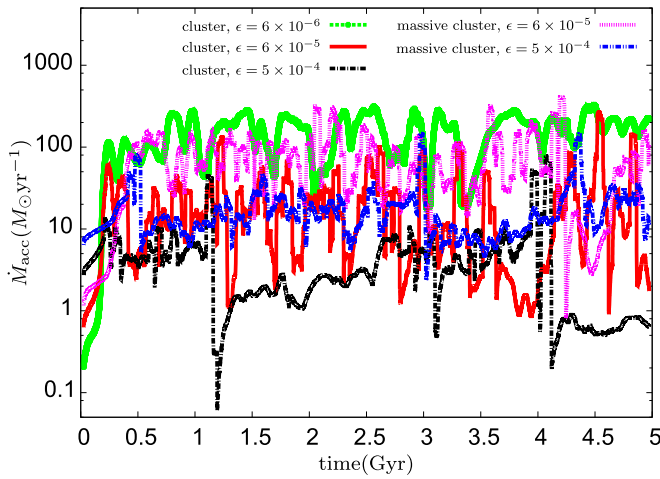
Figure 10. Mass accretion rate through the inner radius (smoothed over 50 Myr) as a function of time for different 2D runs. A lower efficiency and a more massive halo lead to a larger accretion rate.

efficiency ($\epsilon = 5 \times 10^{-4}$), indicated by black dot-dashed line, shows an average accretion rate of 5.1 $M_\odot$ yr^{-1} (about a fifth of the fiducial 2D run; see Table 1); there are far fewer spikes in $\dot{M}_{acc}$ compared to the fiducial run. Similar trends are observed for the massive cluster runs with $\epsilon = 6 \times 10^{-5}$ (magenta dotted line) and 5×10^{-4} (blue double-dot-dashed line). The number of $\dot{M}$ spikes in Figure 10 is smaller for lower halo mass and higher feedback efficiency because of larger overheating and a longer recovery time after a precipitation-induced jet event.

Figure 11 shows the time-averaged (from 4 to 5 Gyr) and emissivity-weighted (0.5–8 keV) 1D profiles of several key quantities for 2D cluster and massive cluster runs with different efficiencies: entropy ($K \equiv T_{keV}/n_e^{2/3}$), t_{cool}/t_{ff}, number density and temperature. All profiles look similar to what is seen in observations. The entropy profile flattens toward the center but the entropy core is prominent only for the higher efficiency (ϵ) runs; a "core" with a constant t_{cool}/t_{ff} is more prominent for lower ϵ and for the massive cluster. As expected, the density is lower and the temperature is higher for a larger feedback heating efficiency. For all efficiencies temperature increases with the radius (except for $\epsilon = 5 \times 10^{-4}$ which is almost isothermal just after a jet outburst; see the top right panel of Figure 12), as seen in the observations of cool-core clusters.

Compared to the cluster runs, the entropy for the massive cluster is higher at larger radii in Figure 11 because the initial entropy was scaled with the halo mass ($K \propto M_{200}^{2/3}$; see Section 2.2). The entropy profiles for the massive cluster runs for the two efficiencies are similar; entropy keeps on decreasing as we go toward the center (forming a "core" in t_{cool}/t_{ff}), more so for $\epsilon = 6 \times 10^{-5}$. As we saw with the mass accretion rate in Figure 10, the effect of increasing the efficiency is similar to that of decreasing the halo mass. This is expected, as the mass accretion rate for lower mass halos is smaller, and the increase in jet efficiency and the consequent higher jet power suppresses accretion.[6]

Another point to note in Figure 11 is that the profiles are rather similar for the massive cluster runs with $\epsilon = 6 \times 10^{-5}$ and 5×10^{-4}. The bottom panels of Figure 12 show that jet events between 4 and 5 Gyr are not able to raise min(t_{cool}/t_{ff})

---

[6] We thank the referee for the suggestion to highlight this point.

much above 10 for these cases. However, the top panels of Figure 12 and the bottom panel of Figure 9 show that between 4 and 5 Gyr min(t_{cool}/t_{ff}) increases with an increasing ϵ. Therefore, the core entropy (density) for the cluster runs increases (decreases) with an increasing ϵ. Note that the core entropy for the cluster runs with a larger efficiency are not always higher; it is only when the core is in the part of the heating cycle with min (t_{cool}/t_{ff}) > 10.

Figure 12 shows various quantities (jet power, cold gas mass and min[t_{cool}/t_{ff}]) as a function of time for 2D cluster ($\epsilon = 10^{-4}$ and 5×10^{-4}; also see the 2D cluster run with $\epsilon = 6 \times 10^{-5}$ in the bottom panel of Figure 9) and massive cluster ($\epsilon = 6 \times 10^{-5}$ and 5×10^{-4}) runs. The first point to note is that the number of jet events (and hence the number of cycles; e.g., see Figure 7) is smaller for a higher efficiency and a lower halo mass. Another is that the peaks in jet power and min(t_{cool}/t_{ff}) for a higher efficiency are larger, resulting in overheating and longer durations for which cold gas and jet power are suppressed. Stronger overheating after jets in higher efficiency (and lower halo mass) runs results because, while the number of cold accretion events is smaller (compared to lower efficiency or a larger halo mass), the mass accretion rate during the multiphase cooling phase is similar (see Figure 10), generally giving larger heating (Equation (6)).

As with the mass accretion rate (see the spikes in Figure 10), for a fixed ϵ the number of cooling/jet events is larger for a massive cluster. While t_{cool}/t_{ff} is $\lesssim$10 and cold gas is present at most times for the massive cluster run with $\epsilon = 6 \times 10^{-5}$, there are longer periods with min[t_{cool}/t_{ff}] $\gtrsim$ 10 and lack of cold gas for the cluster run (see bottom panel of Figure 9). The jet events are more disruptive (as measured by the rise in min[t_{cool}/t_{ff}] after a jet event) in the lower mass halo because the jet power is relatively large but the hot gas mass is smaller (compare the right panels of Figure 12).

4. DISCUSSION AND ASTROPHYSICAL IMPLICATIONS

The cold mode accretion model,[7] in which local thermal instability leads to the condensation and precipitation of cold gas and enhanced accretion onto the SMBH, has emerged as a useful framework to interpret various properties in cores of elliptical galaxies, groups, and clusters (e.g., Pizzolato & Soker 2005; Gaspari et al. 2012; Sharma et al. 2012b; Li & Bryan 2014b). However, there are several unresolved problems: e.g., the role of angular momentum transport, self-gravity and cloud–cloud collisions in accretion onto the SMBH (e.g., Pizzolato & Soker 2010; Hobbs et al. 2011; Babul et al. 2013; Gaspari et al. 2015); relative contribution of cold gas at ~1 kpc to SMBH accretion and star formation; the role of thermal conduction in thermal balance and cold-gas precipitation (Voit et al. 2015; Wagh et al. 2014); the exact mechanism (turbulent mixing, weak shocks; e.g., see Fabian et al. 2003; Dennis & Chandran 2006; Banerjee & Sharma 2014) via which the mechanical power of the jet/cavity is dissipated and distributed throughout the core; and the scaling of various processes with the halo mass.

The key feature of cold mode accretion, unlike the hot mode, is that the mass accretion rate increases abruptly as t_{cool}/t_{ff} becomes smaller than a critical value close to 10. This leads to

---

[7] Here we use the label "cold mode accretion" to refer to the capture and accretion of cold clouds by SMBH, and not the cosmological accretion of cold gas sometimes invoked in halos less massive than $10^{12} M_\odot$ (Birnboim & Dekel 2003).
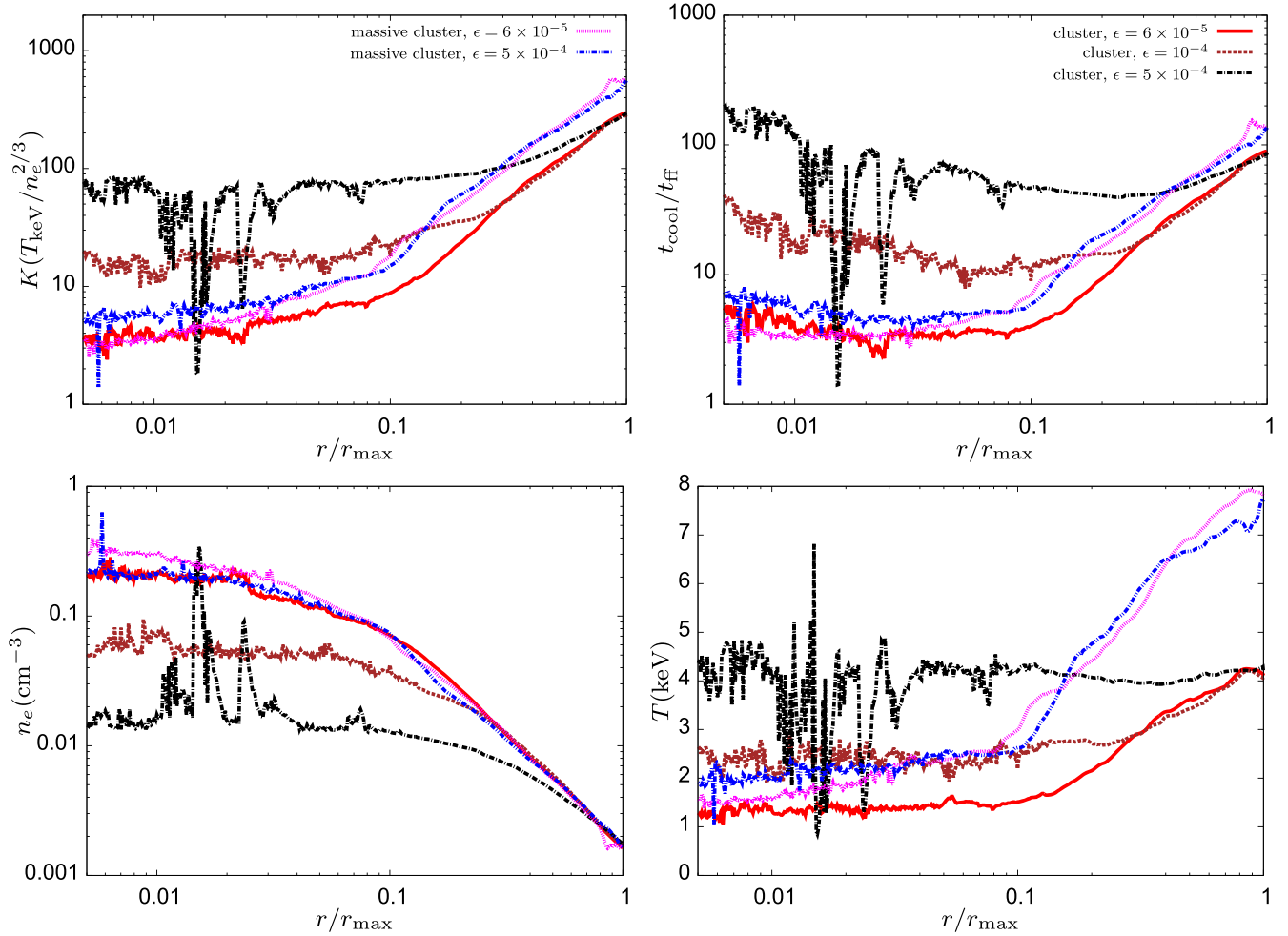
Figure 11. Emissivity-weighted (considering plasma in the range 0.5–8 keV), time (averaged between 4 and 5 Gyr), and angle-averaged profiles for 2D runs as a function of radius scaled to the outer radius (r_{max}): entropy ($K \equiv T_{keV}/n_e^{2/3}$; top left panel); t_{cool}/t_{ff} (top right panel); electron density (n_e; bottom left panel); and temperature (in KeV; bottom right panel). Both min(t_{cool}/t_{ff}) and core entropy decrease for a lower efficiency or a larger halo mass. Temperature is higher for a higher efficiency, but a cool core (a temperature increasing with radius) is preserved for all cases, except for the highest efficiency run. Spikes in the cluster run with $\epsilon = 5 \times 10^{-4}$ signify that there is cool, low entropy gas present in the core from 4 to 5 Gyr.

a strong feedback heating, which temporarily overheats the cluster core. The hot mode feedback, in the form of Bondi accretion onto the SMBH, on the other hand, is not an abrupt switch and increases smoothly with an increasing (decreasing) core density (temperature). In Section 4.1 we discuss the success of the cold accretion model and compare it with previous simulations. In Section 4.2 we compare it with the recent exquisite cold-gas observations and with statistical analyses of X-ray and radio observations of cluster cores.

4.1. Comparison with Previous Simulations

There are two broad categories of jet implementations described in the literature: first, where the jet mass, momentum, and energy are injected via source terms (e.g., Omma et al. 2004; Cattaneo & Teyssier 2007; Gaspari et al. 2012; Li & Bryan 2014a); second, where mass and energy are injected as flux through an inner boundary (e.g., Vernaleo & Reynolds 2006; Sternberg et al. 2007). We use the former approach, which has generally been more successful. In this approach, the sudden injection of kinetic energy after cold gas precipitation leads to a shock which not only expands vertically but also laterally, perpendicular to the direction of momentum

injection. This lateral spread of jet energy and vorticity generation due to interaction with cold clumps help in coupling the jet energy with the equatorial ICM. In the flux-driven approach the jet pressure is usually taken to be the same as ICM pressure and the jet drills a cavity without expanding laterally in the core. Thus, coupling of the jet power is not very effective, unless the jet angle is very broad (Sternberg et al. 2007).

Our jet modeling is similar to the earliest works such as Omma et al. (2004), Omma & Binney (2004), which inject jet mass, momentum, and kinetic energy via source terms. However, this work focused on the effect of a single jet outburst with a fixed power and did not include cooling; the simulations were run for short times ($\lesssim 500$ Myr). Cattaneo & Teyssier (2007) also implement jets using kinetic and thermal energy injection, and run for cosmological timescales. However, they use Bondi prescription for accretion onto the SMBH, and hence their jet power input is tied to cooling and accretion at the center. Since the Bondi radius cannot be resolved in their simulations, they compute the Bondi accretion rate based on the density and temperature at a larger radius. Sometimes (e.g., in Dubois et al. 2010) the Bondi accretion rate evaluated at large radii is artificially enhanced by a factor of ∼100 in order
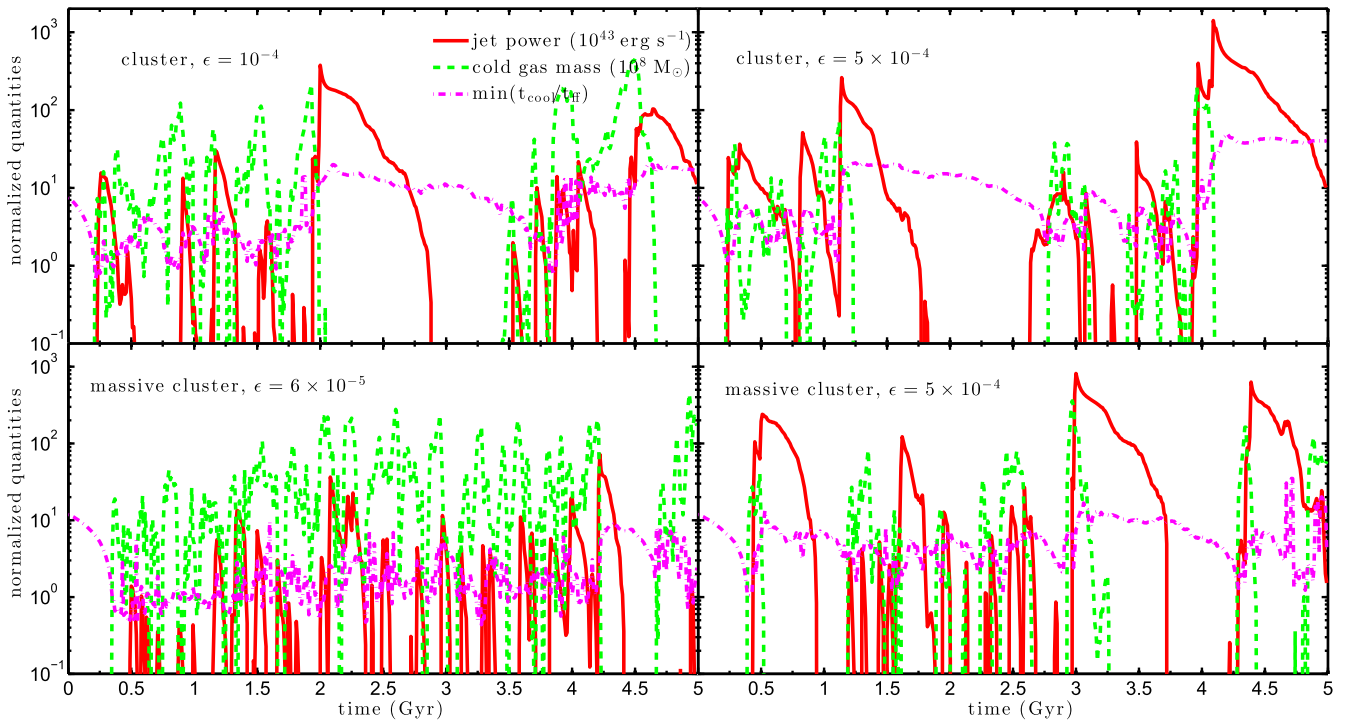
Figure 12. Jet energy, cold gas mass, and $\min(t_{\rm cool}/t_{\rm ff})$ as a function of time for 2D runs with different efficiencies ($\epsilon = 10^{-4}$, 5×10^{-4}, 6×10^{-5}) and halo masses ($M_{200} = 7 \times 10^{14}$, $1.8 \times 10^{15}\,M_{\odot}$). Note that the jet energy and cold gas mass are scaled differently in different panels. A smaller efficiency or a larger halo mass leads to many accretion and jet feedback cycles.

to match feedback heating with cooling. Bondi accretion is only applicable for a smooth, non-rotating gas distribution, and not for clumpy multiphase gas which can accrete at a much higher rate (e.g., Sharma et al. 2012b; Gaspari et al. 2013).

Cielo et al. (2014) have studied the detailed structure and thermodynamics of source-term driven cylindrical jets, of different densities and temperatures, interacting with the ICM but they run for less than 10 Myr. Like us, they also highlight the importance of hot back flows in regulating the central ICM.

Another set of simulations inflates cavities using jets driven by fluxes of mass and momentum at the inner radial boundary (rather than using source terms like us; in cluster context, see Vernaleo & Reynolds 2006; Sternberg et al. 2007; for MHD modeling of the Crab Nebula jet, see Mignone et al. 2013). Vernaleo & Reynolds (2006) injected momentum (and kinetic energy) via the inner radial boundary, with an opening angle of 15°, in the form of 100 times hotter gas but in pressure equilibrium with the ICM. Their jets just drill through a narrow channel without coupling to the catastrophically cooling core. Sternberg et al. (2007) advocated wide (with opening angle $\gtrsim 50°$) boundary-driven jets, such that the jet is not as fast, and can lead to vortices and substantial mixing in cluster cores. However, since their simulations are not run for many cooling times, it is unclear if wide jets and can indeed balance cooling for cosmological times. Moreover, the fat jets may not reproduce the observed morphologies of thin jets and fat bubbles. Using the boundary injection approach, Heinz et al. (2006) emphasize the importance of the dynamic ICM in redistributing jet energy but they also run for less than a cooling time.

Recent numerical simulations of AGN-driven jets (Gaspari et al. 2012; Li & Bryan 2014a, 2014b) have been quite successful in producing several observed features such as the

lack of plasma cooling below a third of the ICM temperature (Figure 11 in Li & Bryan 2014b), suppression of cooling and accretion in the core (by a factor of 10–100 relative to a cooling flow), maintenance of cool-core structure even with strong intermittent jet events, formation of an angular momentum supported cold-gas torus, viability of AGN feedback from elliptical galaxies to massive clusters. Our simulations are different from these recent works, which use mesh refinement in a cartesian geometry, in that we use a spherical coordinate system. We have also tried to push the AGN feedback efficiency toward the lower limit, which is still able to suppress a cooling flow. We find that an efficiency $\epsilon = 6 \times 10^{-5}$ is able to suppress a cluster cooling flow by a factor of 10.

Like us, Gaspari et al. (2012) and Li & Bryan (2014b) also make an estimate of the mass accretion rate onto the SMBH. Gaspari et al. (2012) consider a spherical shell of radius 0.5 kpc and calculate the mass accretion rate ($\dot{M}_{\rm acc}$) due to infalling gas. Li & Bryan (2014b), Li et al. (2015) calculate the mass accretion rate ($\dot{M}_{\rm acc}$) by dividing the cold gas mass within 0.5 kpc by 5 Myr (of order the dynamical timescale). Our estimate of $\dot{M}_{\rm acc}$ is similar to Gaspari et al. (2012), except that we calculate it at 1 kpc. Only a small fraction of $\dot{M}_{\rm acc}$ is expected to be accreted onto the SMBH; thus, the efficiency factor (ϵ) in Equation (6) takes into account both the fraction of $\dot{M}_{\rm acc}$ that is accreted by the SMBH and the efficiency of converting SMBH accretion into jet mechanical energy.

While our jet feedback implementation is very similar to Gaspari et al. (2012), our results differ in some key respects. The main difference is that we see extended cold gas and jet/cold-gas cycles even at late times (see Figures 1, 3, 7, 9). Like Li & Bryan (2014b), in Gaspari et al. (2012) there is a long-lived rotationally supported torus at a few kpc and the extended multiphase gas is lacking at later times (see their Figures 10 and

11). The main reason for the absence of extended cold gas and strong jets at late times in previous simulations is a large feedback efficiency. A larger feedback efficiency leads to very strong feedback heating at early times, and the core reaches rough thermal balance in a state of $t_{cool}/t_{ff} > 10$ with no fresh extended (radially dominant) cold gas condensing at late times. Since a large fraction of cool core clusters show extended cold gas (McDonald et al. 2011a), a smaller value of feedback efficiency seems more consistent with observations.

To solve the problem of a steady cold torus present at late times, very recently, Li et al. (2015) have incorporated the depletion of cold gas via star formation in the core, but they adopt the same feedback prescription as in their previous works. Star formation exhausts the amount of cold gas within 0.5 kpc, suppresses AGN heating, and leads to a cooling event after which cold gas condenses again. Thus, they obtain three cooling-feedback cycles in their fiducial run. In their AGN feedback prescription, star formation efficiency primarily determines the frequency of cooling/heating cycles. In contrast, our cycles are determined by the AGN feedback efficiency and the halo mass (more cycles for a massive halo and a smaller feedback efficiency). While there is some ongoing star formation in cool cluster cores, Li et al. (2015) form $3 \times 10^{11} M_\odot$ in stars over 6.5 Gyr for their fiducial run corresponding to the Perseus cluster, a significant fraction of the mass of the BCG (brightest cluster galaxy; $8 \times 10^{11} M_\odot$; Lim et al. 2008). This does not agree with semi-analytic models, which suggest that 80% of the stars of BCGs are assembled before $z = 3$ (i.e., only $2 \times 10^{10} M_\odot$ are expected to form over the past 12 Gyr; De Lucia & Blaizot 2007). Moreover, the current star formation rate even in the most extreme cool core clusters is typically $\lesssim 10 M_\odot$ yr^{-1} (Hicks et al. 2010; McDonald et al. 2011b); the average star formation rate of Li et al. (2015) would correspond to an unacceptably high value, $\approx 46 M_\odot$ yr^{-1}.

We can directly compare our results with Gaspari et al. (2012), as our feedback prescription is similar. They tried jet efficiency factors of $\epsilon = 6 \times 10^{-3}$, 0.01. With a much higher accretion efficiency ($\epsilon = 0.01$) compared to ours ($\sim 10^{-4} - 10^{-5}$), Gaspari et al. (2012) get a larger suppression factor ($\dot{M}_{acc}/\dot{M}_{cf} \sim 1\% - 2\%$) compared to us, as expected. Gaspari et al. (2012) use a halo mass $M_{200} \sim 10^{15} M_\odot$. Figure 8 shows how our results compare with Gaspari et al. (2012). The suppression factor of a massive cluster ($M_{200} = 1.7 \times 10^{15} M_\odot$) for our fiducial $\epsilon = 6 \times 10^{-5}$ is 20%, larger than their work. Suppression factor in our massive cluster (cluster) run for $\epsilon = 0.01$, as seen in Figure 8, is 3% (0.8%), in rough agreement with the results of Gaspari et al. (2012).

4.2. Comparison with Observations

Now that we have done some comparisons with previous simulations, in this section we compare our results with observations. We note that the observational comparison may not be perfect because our simulations lack some physical processes such as magnetic fields and thermal conduction. These effects will be considered later. Moreover, observations suffer from projection effects, and our cluster parameters do not span as broad a range (of halo masses, entropy profiles at large radii, etc.) as encountered in observations.

One of the most commonly studied ICM properties is its entropy profile (e.g., Cavagnolo et al. 2009). Figure 11 shows the time averaged (4–5 Gyr), X-ray emissivity weighted

profiles of t_{cool}/t_{ff} and entropy as a function of radius for our various runs. We see that an entropy core (with a prominent local minimum in t_{cool}/t_{ff}) is a good approximation for systems in which $t_{cool}/t_{ff} \gtrsim 10$ and there is no extended cold gas. This state is common for simulations with larger efficiency and lower halo mass. However, the halos with $t_{cool}/t_{ff} < 10$, in which there is lot of currently condensing and infalling cold gas, are consistent with a "core" in t_{cool}/t_{ff} and a decreasing entropy toward the cluster center, albeit with a shallower slope. This is consistent with recent reanalysis of core entropy profiles (Panagoulia et al. 2014), which suggests that a double power-law entropy profile, with a shallower entropy in the center, better describes the ICM core. It will be useful to compare the behavior of central entropy as a function of $\min(t_{cool}/t_{ff})$; we expect entropy cores for $\min(t_{cool}/t_{ff}) > 10$ and slowly increasing entropy profiles for $\min(t_{cool}/t_{ff}) \lesssim 5$.

Figures 13 and 14 show the correlation between various important quantities for our 2D cluster runs (with $\epsilon = 6 \times 10^{-5}$, 10^{-4}, 5×10^{-4}) and the 3D fiducial run, respectively. Data points sampled every 10 Myr are shown. The core entropy (K_0) is obtained by using a least squares fit to the emissivity-weighted 1D entropy profile of gas in 0.5–8 keV range. In both these figures the strongest correlation is between K_0 and $\min(t_{cool}/t_{ff})$, as expected, because both these quantities depend on density and temperature in a similar way ($K \propto T/n^{2/3}$ and $t_{cool}/t_{ff} \propto T^{1/2}/n$; see Equation (35) in McCourt et al. 2012); the relation is not one-to-one because K_0 is determined by entropy near the center and $\min(t_{cool}/t_{ff})$ by the behavior at the core radius (beyond which density decreases sharply).

The spread in the $K_0 - \min(t_{cool}/t_{ff})$ correlation is larger for a lower K_0 (or equivalently, $\min[t_{cool}/t_{ff}]$; this is also seen in observational data shown in Figure 4 in Voit et al. 2015) because a core with constant entropy is not a good description in that case and the entropy decreases inward (see top left panel of Figure 11).

The correlation between various quantities in Figures 13 and 14 are not particularly strong because of the hysteresis behavior of various quantities (e.g., jet power, radially dominant cold gas mass) with respect to the core properties (Figure 7). Figures 13 and 14 show that, in general, the jet power increases for a larger K_0 (or $\min[t_{cool}/t_{ff}]$), particularly for a larger core entropy. This is because a large jet power overheats the cluster core and raises its entropy. Other quantities do not show such strong correlations in these plots; cold gas mass increases with a lower entropy or a shorter cooling time, but jet energy and cold gas mass show a large spread relative to each other (since cold gas leads to increase in jet energy, which in turn suppresses cold gas mass).

The 3D run shown in Figure 14 prominently shows the sign of the massive torus at late times. Apart from this, there are no major differences in 2D and 3D. Also note that cold gas is missing in the $\epsilon = 5 \times 10^{-4}$ 2D cluster run for $t_{cool}/t_{ff} \gtrsim 20$ (Figure 13; the same is expected for the radially dominant cold gas in 3D). This is consistent with the observations of Cavagnolo et al. (2008), who find that Hα luminosity is suppressed for a core entropy >30 keV cm^2 (corresponding to $\min[t_{cool}/t_{ff}]$ of about 20; see the top right panel of Figure 13 and Figure 4 in Voit et al. 2015). The onset of star formation in cluster cores also happens sharply below the same entropy threshold (Rafferty et al. 2008). Figure 14 shows that the core entropy and $\min(t_{cool}/t_{ff})$ remain below 20 even if the

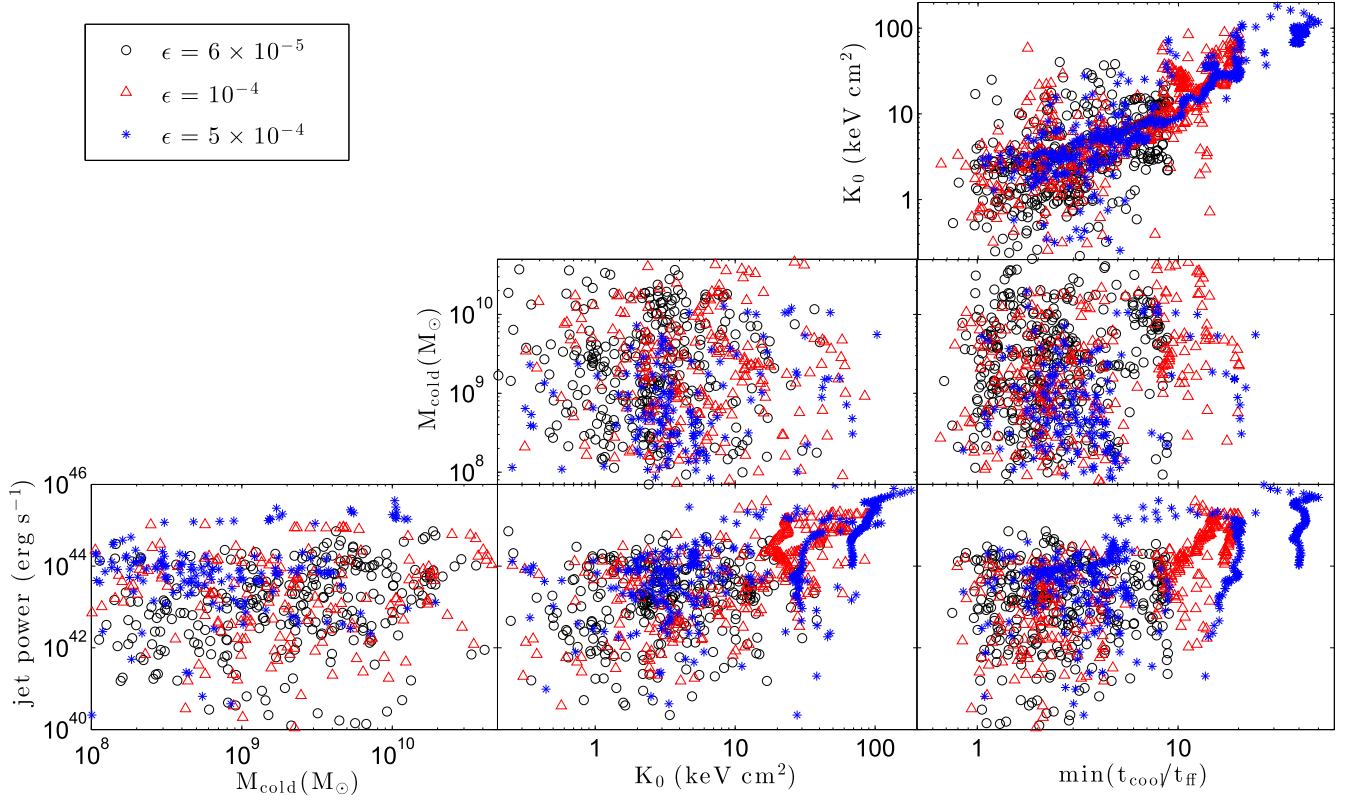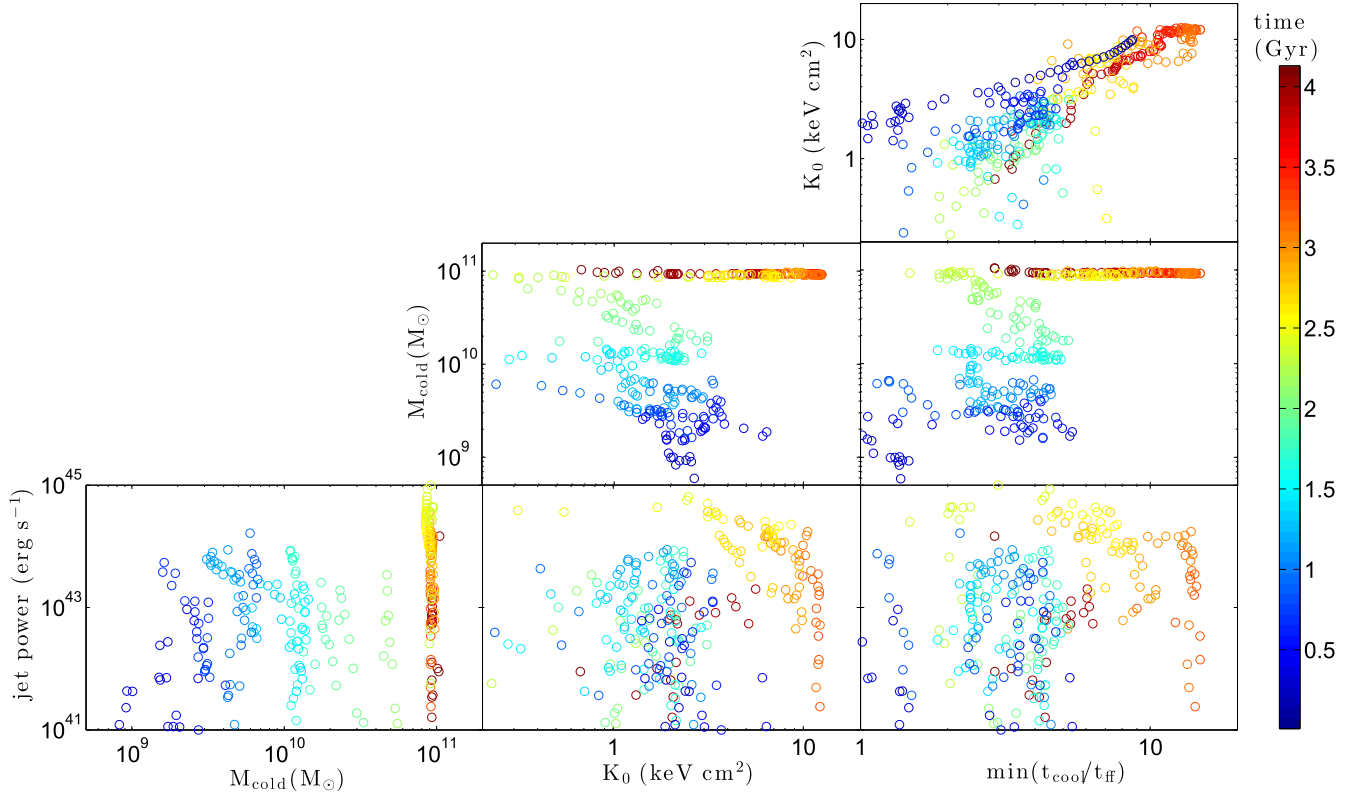**Figure 13.** Various important quantities measured at the same time (jet energy, cold gas mass, core entropy, and $\min[t_{\rm cool}/t_{\rm ff}]$) plotted against each other from our 2D cluster runs with different efficiencies. The data is sampled every 10 Myr. There is a strong correlation between the core entropy and $\min(t_{\rm cool}/t_{\rm ff})$, especially at larger values of $\min(t_{\rm cool}/t_{\rm ff})$. There is also a positive correlation between K_0-jet energy and $\min(t_{\rm cool}/t_{\rm ff})$-jet power. Larger efficiency runs lead to a larger value of $\min(t_{\rm cool}/t_{\rm ff})$ and K_0. Notice that cold gas is absent if $\min(t_{\rm cool}/t_{\rm ff}) \gtrsim 30$.

Figure 14. Important quantities measured at the same time (jet energy, cold gas mass, core entropy, and $\min[t_{\rm cool}/t_{\rm ff}]$) plotted against each other in our fiducial 3D cluster run. As in 2D runs (see Figure 13), there is a strong correlation between K_0-$\min(t_{\rm cool}/t_{\rm ff})$, K_0-jet power, and $\min(t_{\rm cool}/t_{\rm ff})$-jet energy. The cold gas mass is high and becomes almost constant at later times, as seen in the top panel of Figure 9. The color-coding corresponds to time.
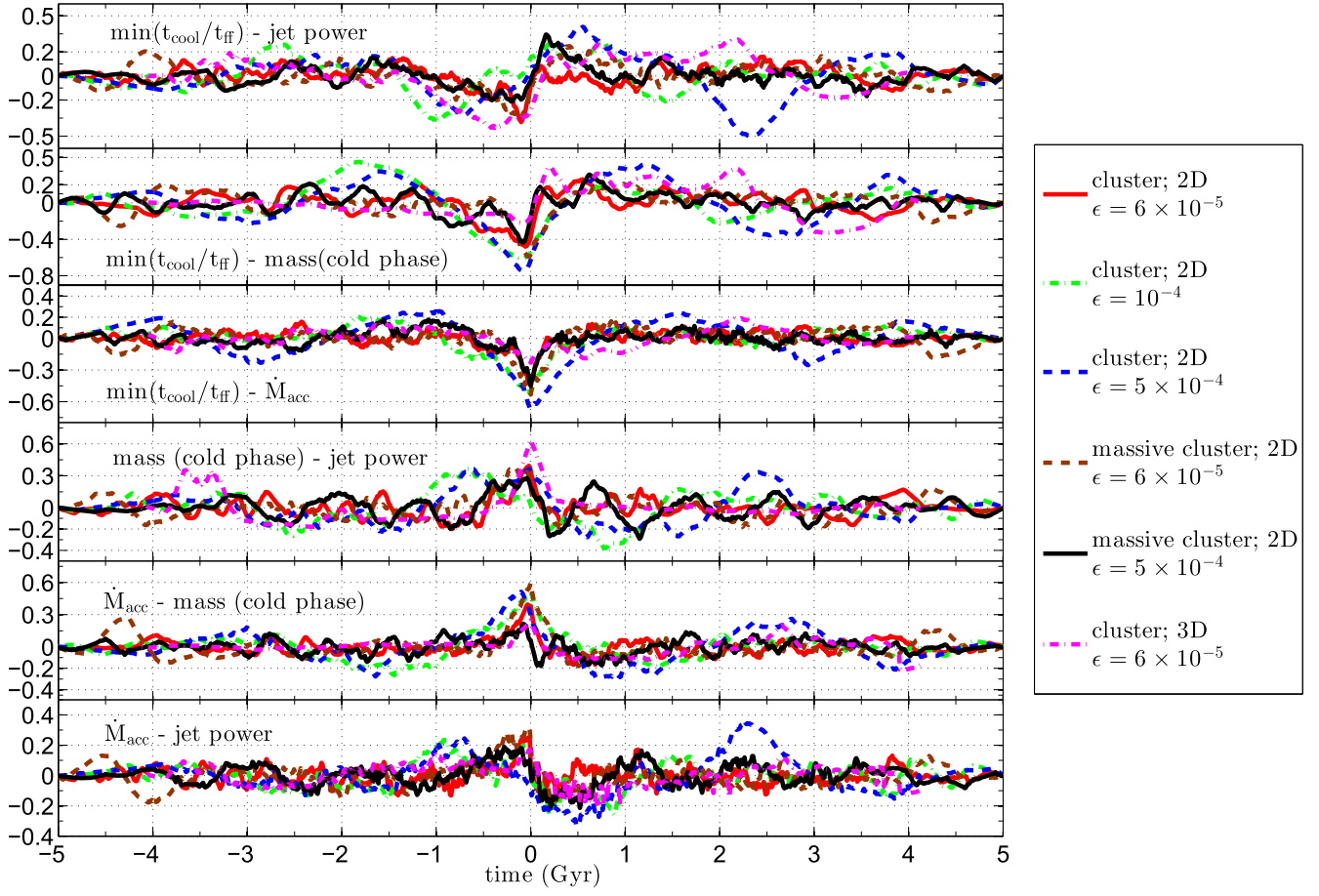
Figure 15. Cross-covariance of various quantities ($\min[t_{\rm cool}/t_{\rm ff}]$, jet energy, mass in cold phase, $\dot{M}_{\rm acc}$) as a function of time lag to show temporal relationship between these various quantities. Cross covariance between two quantities as a function of time, as used here, is defined as: $\text{cov}(a, b; \tau) = \int_0^{T-|\tau|} [\delta a(t + \tau)\delta b(t)dt] / \left[\sqrt{\int_0^T |\delta a(t)|^2 dt \int_0^T |\delta b(t)|^2 dt} \right]$, where $-T \leqslant \tau \leqslant T$ is the time lag and δa and δb are mean-subtracted quantities. Since there is a large variation in various quantities (see Figures 13 and 14), we take log before evaluating cross-covariance. For the 3D cluster run we have used the radially dominant cold gas mass; the cross-covariance is much weaker if we use total cold gas mass.

instantaneous jet power is as high as $10^{45}\,\text{erg s}^{-1}$; core entropy can be much higher (up to $100\,\text{keV cm}^2$) for higher efficiency (see $\epsilon = 5 \times 10^{-4}$ in Figure 13).

While Figures 13 and 14 show correlations between various quantities at a given time, we are also interested in understanding causal relationships between various quantities such as cold gas mass, $\min(t_{\rm cool}/t_{\rm ff})$, and jet energy. Figure 15 shows the temporal cross-covariance between various important parameters (we take log before calculating cross-covariance). Various 2D and 3D simulations with different efficiencies are plotted together. The trends that are common to all simulations are likely to be robust. Robust correlations among various quantities occur only with a time lag <1 Gyr (typical core cooling/heating time).

The top three panels in Figure 15 show that the cross-covariance between $\min(t_{\rm cool}/t_{\rm ff})$ decreases ~ 0.5 Gyr before zero lag and rises for 0.5 Gyr after that (rise is not so prominent with $\dot{M}_{\rm acc}$). The interpretation is that the cooling time (and hence $\min[t_{\rm cool}/t_{\rm ff}]$) decreases as the core cools during the cooling leg of the cycle. This leads to the condensation of radially dominant cold gas after a cooling time (few 100 Myr) and an enhancement of the mass accretion rate and the jet power. Sudden increase in jet power overheats the core and $\min$

($t_{\rm cool}/t_{\rm ff}$) increases after a lag of few 100 Myr; cold gas mass and $\dot{M}_{\rm acc}$ also decrease consequently.

The bottom three panels in Figure 15 show that cold gas mass (radially dominant), mass accretion rate, and jet power are positively correlated. A slight skew toward a negative time lag shows that the cold gas mass and the mass accretion rate increases first, and that gives rise to an increase in jet power. Thus, the cross-covariance behavior of different variables is similar to that seen in cold gas-jet cycles in Figure 7. Also note in Figure 15 that there are smaller number of oscillations for higher feedback efficiency (or smaller halo mass); this is a reflection of smaller number of cooling/feedback cycles in these cases (see Figure 12).

In our 3D simulations we see the build-up of a massive rotationally supported torus. A part of this torus should cool further and lead to star formation, as argued by Li et al. (2015). While the cold gas (mostly in the torus) builds up in time and saturates after 2 Gyr, the jet energy shows fluctuations in time even after that (see the top panel of Figures 9 and 14). Therefore, in our models there is no correlation between *total* cold gas mass and jet energy. However, there is a correlation between the radially dominant cold gas mass and the jet energy (compare the green-dotted and black dot-dashed lines in the top panel of Figure 9). Thus, although most cold gas is decoupled

from jet feedback, it is the subdominant *infalling cold gas* that is powering AGNs. This is in line with the observations of McNamara et al. (2011), who find no correlation between the jet power and the available molecular gas. They therefore argue that most of the cold gas is converted into stars rather than accreted by the SMBH.

Finally, we compare our simulations with recent observational studies of cold gas kinematics and star formation. These have been studied in unprecedented detail in some elliptical galaxies and clusters, thanks mainly to *ALMA* and *Herschel* telescopes (e.g., Edge et al. 2010; Rawle et al. 2012; Tremblay et al. 2012; David et al. 2014; McNamara et al. 2014; Russell et al. 2014; Werner et al. 2014). In this paper we have mainly focussed time-averaged kinematics, as shown in Figures 4 and 5. We can clearly see three kinematically distinct components of cold gas: a rotationally supported massive torus, ballistically infalling cold gas, and jet-uplifted fast cold gas.

Observations of different clusters are snapshots at a particular instant, at which a particular component (e.g., the rotating torus, a fast outflow, or a radially distributed inflow; see Figure 6) of the cold gas distribution may be more prominent. We will present the details of cold gas kinematics in various states of the ICM (with cold inflows, outflows, and the rotating torus) in a future work.

Some of the salient properties of the cold gas distribution in the fiducial run are: the rotating cold gas torus, when present, is more massive compared to infalling cold gas (this component may be exaggerated in our simulations as we do not include star formation that would quickly consume some of the cold gas); the rotating disk rotates at the almost constant local circular velocity (100–200 km s^{-1} for our fiducial cluster run; the actual value may be larger because we have ignored the gravitational potential due to the BCG) in form of a massive torus within 5 kpc; the radially dominant cold gas is much more spatially extended (out to few 10s of kpc) compared to the rotating torus, and the majority of this component also has a velocity close to the circular velocity; some (about $10^5 \, M_\odot$) radially dominant outflowing gas has a radial velocity as high as 1000 km s^{-1} (a fast component is seen in the observations of Russell et al. 2014 and McNamara et al. 2014); the infalling cold gas (on average) is about twice as much as the outflowing component.

While the accretion rate through the inner radius (dominated by cold gas) is smaller than 100 $M_\odot$ yr^{-1} (the accretion rate onto the SMBH is $\lesssim$1% of this) at all times (see Figure 9), the cooling/accretion and outflow rates in the cold gas can be much larger instantaneously because of the massive cold torus buffer (Figure 6).

The observations show varying cold gas kinematics in different systems: radially infalling cold molecular clouds of 3×10^5 to $10^7 \, M_\odot$ in a galaxy group NGC 5044 (David et al. 2014); $5 \times 10^{10} \, M_\odot$ molecular gas predominantly in a rotating disk, and about $10^{10} \, M_\odot$ in a fast (line of sight velocity up to 500 km s^{-1}) outflow in Abell 1835 (McNamara et al. 2014); $10^{10} \, M_\odot$ of molecular gas roughly equally divided between as rotating disk (velocity $\sim$250 km s^{-1}) and a faster (570 km s^{-1}) infalling/outflowing component in Abell 1664 (Russell et al. 2014). In our simulations we observe similar components of the cold gas distribution, as shown in Figures 4 and 5.

5. CONCLUSIONS

Cold-mode feedback, due to condensation of cold gas from the hot ICM when the local density is higher than a critical value (see below), has emerged as an attractive paradigm to interpret observations in cluster cool cores. In this paper we have carried out simulations of clusters of halo masses $7 \times 10^{14} \, M_\odot$ and $1.8 \times 10^{15} \, M_\odot$ with feedback driven AGN jets, varying the feedback efficiency over a large range ($10^{-5} - 0.01$). AGN feedback is able to suppress cooling flows within the observational limits (by a factor of $\sim$10) even for a feedback efficiency as low as 6×10^{-5}. This is the major difference from previous jet simulations, which use a much larger feedback efficiency ($\gtrsim 10^{-3}$; Gaspari et al. 2012; Li & Bryan 2014b; Li et al. 2015). Because of the high feedback efficiency, the previous simulations attain thermal equilibrium in a hot, low-density core (with $t_{cool}/t_{ff} > 10$) which does not show cold gas and jet cycles at late times. In contrast, our low efficiency simulations show cooling/jet cycles even at late times.

The core undergoes cooling and feedback heating cycles because of cold gas precipitation and enhanced accretion onto the SMBH. There are more cycles for a lower efficiency and a larger halo mass. The cool-core appearance is preserved even during strong jet events. Even with large efficiencies, jet feedback raises the core entropy to several tens of keV cm^2, and therefore cannot explain the non-cool-core clusters with large cores and entropies greater than 100 keV cm^2. The origin of these non-cool-core clusters is still poorly understood (see, e.g., Poole et al. 2008).

In this paper we highlight some results that were not emphasized in previous simulations of AGN jet feedback in clusters; in particular, we compare our results with several recent observations. The following are our major conclusions.

1. First and most importantly, the results from different codes, different setups, and different implementation of jet feedback (as long as condensation and accretion of cold gas are accounted for; e.g., Gaspari et al. 2012; Li et al. 2015) give qualitatively similar results. This indicates the robustness of the cold feedback mechanism, and the importance of precipitation (which occurs when $t_{cool}/t_{ff} \lesssim 10$) and associated feedback in regulating cluster cores.

2. We find that a feedback efficiency (defined as the ratio of jet mechanical luminosity and the rest mass accretion rate [$\dot{M}_{acc} c^2$] at $\sim$1 kpc; see Equation (6)) of as small as 6×10^{-5} is sufficient to suppress the cooling/star formation rate in cluster cores by a factor of about 10 (see Figure 8). An even smaller efficiency is sufficient for lower mass halos because the thermal energy of the ICM is smaller compared to the rest mass energy. Our fiducial efficiency is at least 20 times lower than the models of Li & Bryan (2014b) and Gaspari et al. (2012). Our values are consistent with the expectation that the mass accretion rate onto the SMBH is much smaller than the accretion rate estimated at $\sim$1 kpc, and the fact that powerful jets exist only when the SMBH accretion rate is smaller than 0.01 time the Eddington rate.

The required efficiency can be roughly estimated as follows. On average, the core luminosity is balanced by the energy input rate; i.e., $\epsilon_{req} \dot{M}_{acc} c^2 \sim L_X$ (ϵ_{req} is the required feedback efficiency, $\dot{M}_{acc}$ is the accretion rate

estimated at 1 kpc, and L_X is the X-ray luminosity of the cooling core). If we assume that the mass accretion rate is a fixed factor f ($\ll 1$) of the cooling flow value then,

$$\epsilon_{\rm req} f \frac{M_c c^2}{t_{\rm cool}} \approx \frac{1.5 k_B T M_c}{\mu m_p t_{\rm cool}}$$

(M_c is the core mass) implies that

$$\epsilon_{\rm req} \approx \frac{c_s^2}{f c^2} \approx 3 \times 10^{-5} \left(\frac{f}{0.1} \right)^{-1} \left(\frac{M_{200}}{7 \times 10^{14} \, M_\odot} \right)^{2/3},$$

normalizing to the parameters of our fiducial cluster ($T = 2$ keV; see the bottom right panel of Figure 11), where $c_s^2 = k_B T / \mu m_p$ is the sound speed of the core ICM. This estimate agrees with our fiducial efficiency $\epsilon = 6 \times 10^{-5}$.

3. We observe cycles in jet energy, radially dominant cold gas mass, and mass accretion rate which are governed by $t_{\rm cool}/t_{\rm ff}$ measured in the hot phase. If $t_{\rm cool}/t_{\rm ff} \lesssim 10$ cold gas precipitates, and leads to multiphase cooling and enhanced accretion onto the SMBH. Sudden rise in the accretion rate, for a sufficiently high feedback efficiency, leads to overheating of the core and an increase in $t_{\rm cool}/t_{\rm ff}$ above the threshold for cold gas condensation. We emphasize that thermal equilibrium in cluster cores only holds in a time-averaged sense. There are cooling/heating cycles during which the core slowly cools/heats up. The core spends a longer time in the hot state for a larger feedback efficiency and a lower halo mass, leading to a smaller number of cooling/heating cycles (see Figure 12).

Several observations hint at cycles in jet power and cooling of the hot gas (see Figure 7). We do not expect such cycles if feedback occurs via the smooth hot/Bondi mode as we do not have sudden cooling/feedback events. The hysteresis behavior observed in the core X-ray properties (K_0, min[$t_{\rm cool}/t_{\rm ff}$]) and the mass of cold gas, jet power, etc. leads to a large dispersion in the correlation between these quantities (see Figures 13 and 14). In particular, the mass accretion rate (at 1 kpc) is independent of the *total* cold gas mass, which is dominated by the rotating cold torus, most of which is consumed by star formation (rather than accretion onto SMBH; e.g., McNamara et al. 2011).

4. We can classify the cold gas in our 3D simulations into two spatially and kinematically distinct components: a centrally concentrated (within 5 kpc), rotationally supported ($|v_\phi| \gg |v_r|$) torus (Figure 3); and extended (both infalling and outgoing) cold gas going out to 30 kpc (Figure 4). The massive, rotationally supported disk is decoupled from the feedback loop; the radially dominant infalling cold gas is what closes the feedback cycle. The cold torus rotates at the local circular speed (200–300 km s^{-1}). The infalling cold gas can be fast ($\lesssim 400$ km s^{-1}), but the uplifted cold gas from the rotating torus can sometimes reach speeds larger than 1000 km s^{-1} as it is accelerated by the fast jet (Figure 5). The mass of the radially dominant infalling cold gas is about a factor of two times the outflowing cold gas. The massive cold torus is expected to be substantially depleted by star formation, which we do not take into account in our simulations.

5. The minimum in the ratio of the cooling time and the free fall time (min[$t_{\rm cool}/t_{\rm ff}$]) seems better than the core entropy (K_0) for characterizing the cool cores. First of all it is a dimensionless parameter which applies for all halo masses (Voit et al. 2015), and second it is not sensitive to strong cooling or heating in the very center (unlike K_0). The entropy and $t_{\rm cool}/t_{\rm ff}$ panels in Figure 11 show that a constant $t_{\rm cool}/t_{\rm ff}$ "core," which corresponds to a double power law for the entropy profile (with a slow increase with radius in the core; as argued in Panagoulia et al. 2014), is a better approximation to clusters in the very cool state with min($t_{\rm cool}/t_{\rm ff}$) $\lesssim 5$.

REFERENCES

Babul, A., Balogh, M. L., Lewis, G. F., & Poole, G. B. 2002, MNRAS, 330, 329
Babul, A., Sharma, P., & Reynolds, C. S. 2013, ApJ, 768, 11
Balogh, M. L., Babul, A., & Patton, D. R. 1999, MNRAS, 307, 463
Banerjee, N., & Sharma, P. 2014, MNRAS, 443, 687
Benson, A. J., & Babul, A. 2009, MNRAS, 397, 1302
Bildfell, C., Hoekstra, H., Babul, A., & Mahdavi, A. 2008, MNRAS, 389, 1637
Binney, J., & Tabor, G. 1995, MNRAS, 276, 663
Birnboim, Y., & Dekel, A. 2003, MNRAS, 345, 349
Bîrzan, L., Rafferty, D. A., McNamara, B. R., Wise, M. W., & Nulsen, P. E. J. 2004, ApJ, 607, 800
Böhringer, H., Matsushita, K., Churazov, E., Ikebe, Y., & Chen, Y. 2002, A&A, 382, 804
Cattaneo, A., & Teyssier, R. 2007, MNRAS, 376, 1547
Cavagnolo, K. W., Donahue, M., Voit, G. M., & Sun, M. 2009, ApJS, 182, 12
Cavagnolo, K. W., Donahue, M., Voit, M., & Sun, M. 2008, ApJL, 683, L107
Cielo, S., Antonuccio-Delogu, V., Macció, A. V., Romeo, A. D., & Silk, J. 2014, MNRAS, 439, 2903
Ciotti, L., & Ostriker, J. 2001, ApJ, 551, 131
Crawford, C. S., Allen, S. W., Ebeling, H., Edge, A. C., & Fabian, A. C. 1999, MNRAS, 306, 857
David, L. P., Lim, J., Forman, W., et al. 2014, ApJ, 792, 94
De Lucia, G., & Blaizot, J. 2007, MNRAS, 375, 2
Dekel, A., & Birnboim, Y. 2008, MNRAS, 383, 119
Dennis, T. J., & Chandran, B. D. G. 2006, ApJ, 622, 205
Donahue, M., Mack, J., Voit, G. M., et al. 2000, ApJ, 545, 670
Dubois, Y., Devriendt, A., Slyz, A., & Teyssier, R. 2010, MNRAS, 409, 985
Edge, A. C. 2001, MNRAS, 328, 762
Edge, A. C., Oonk, J. B. R., Mittal, R., et al. 2010, A&A, 518, L46
Fabian, A. C. 1994, ARAA, 32, 277F
Fabian, A. C., Sanders, J. S., Allen, S. W., et al. 2003, MNRAS, 344, L43
Gaspari, M., Brighenti, F., & Temi, P. 2015, A&A, 579, 62
Gaspari, M., Ruszkowski, M., & Oh, S. P. 2013, MNRAS, 432, 3401
Gaspari, M., Ruszkowski, M., & Sharma, P. 2012, ApJ, 746, 94
Hayes, J. C., Norman, M. L., Fiedler, R. A., et al. 2006, ApJS, 165, 188
Heinz, S., Brüggen, M., Young, A., & Levesque, E. 2006, MNRAS, 373, L65
Hicks, A. K., Mushotzky, R., & Donahue, M. 2010, ApJ, 719, 1844
Hobbs, A., Nayakshin, S., Power, C., & King, A. 2011, MNRAS, 413, 2633
Kaiser, N. 1986, MNRAS, 222, 323
Kaiser, N. 1991, ApJ, 383, 104
Lewis, G. F., Babul, A., Katz, N., et al. 2000, ApJ, 536, 623
Li, Y., Bryan, G., Ruszkowski, M., et al. 2015, arXiv:1503.02660
Li, Y., & Bryan, G. L. 2014a, ApJ, 789, 153
Li, Y., & Bryan, G. L. 2014b, ApJ, 789, 54
Lim, J., Ao, Y., & Dinh-V-Trung 2008, ApJ, 672, 252
Loewenstein, M., Mushotzky, R. F., Angelini, L., Arnaud, K. A., & Quataert, E. 2001, ApJL, 555, L21
McCarthy, I. G., Babul, A., Bower, R. G., & Balogh, M. L. 2008, MNRAS, 386, 1309
McCourt, M., Sharma, P., Quataert, E., & Parrish, I. J. 2012, MNRAS, 419, 3319

McDonald, M., Veilleux, S., & Mushotzky, R. 2011a, ApJ, 731, 33
McDonald, M., Veilleux, S., Rupke, D. S. N., & Mushotzky, R. 2010, ApJ, 721, 1262
McDonald, M., Veilleux, S., Rupke, D. S. N., Mushotzky, R., & Reynolds, C. S. 2011b, ApJ, 734, 95
McNamara, B. R., & Nulsen, P. E. J. 2007, ARA&A, 45, 117
McNamara, B. R., Rohanizadegan, M., & Nulsen, P. E. J. 2011, ApJ, 727, 39
McNamara, B. R., Russell, H. R., Nulsen, P. E. J., et al. 2014, ApJ, 785, 44
Merloni, A., Heinz, S., & Di Matteo, T. 2003, MNRAS, 345, 1057
Mignone, A., Striani, E., Tavani, M., & Ferrari, A. 2013, MNRAS, 436, 1102
Mittal, R., Hudson, D. S., Reiprich, T. H., & Clarke, T. 2009, A&A, 501, 835
Narayan, R., & Yi, I. 1995, ApJ, 444, 231
Navarro, J. F., Frenk, C. S., & White, S. D. 1996, ApJ, 462, 563
O'Dea, C. P., Baum, S. A., Privon, G., et al. 2008, ApJ, 681, 1035
Omma, H., & Binney, J. 2004, MNRAS, 350, L13
Omma, H., Binney, J., Bryan, G., & Slyz, A. 2004, MNRAS, 348, 1105
O'Sullivan, E., Combes, F., Hamer, S., et al. 2015, A&A, 573, A111
Panagoulia, E. K., Fabian, A. C., & Sanders, J. S. 2014, MNRAS, 438, 2341
Peterson, J. R., Kahn, S. M., Faerels, F. B. S., et al. 2003, ApJ, 590, 207
Pizzolato, F., & Soker, N. 2005, ApJ, 632, 821
Pizzolato, F., & Soker, N. 2010, MNRAS, 408, 961
Ponman, T. J., Cannon, D. B., & Navarro, J. F. 1999, Natur, 397, 135
Poole, G. B., Babul, A., McCarthy, I. G., Sanderson, A. J. R., & Fardal, M. A. 2008, MNRAS, 391, 1163
Pope, E. C. D., Babul, A., Pavlovski, G., Bower, R. G., & Dotter, A. 2010, MNRAS, 406, 2023
Pratt, G. W., Croston, J. H., Arnaud, M., & Böhringer, H. 2009, A&A, 498, 361
Rafferty, D. A., McNamara, B. R., & Nulsen, P. E. J. 2008, ApJ, 687, 899
Rawle, T. D., Edge, A. C., Egami, E., et al. 2012, ApJ, 747, 29

Revaz, Y., Combes, F., & Salomé 2008, A&A, 477, L33
Robertson, B. E., Kravtsov, A. V., Gnedin, N. Y., Abel, T., & Rudd, D. H. 2010, MNRAS, 401, 2463
Russell, H. R., McNamara, B. R., Edge, A. C., et al. 2014, ApJ, 784, 78
Salomé, Combes, F., Edge, A. C., et al. 2006, A&A, 454, 437
Saro, A., Borgani, S., Tornatore, L., et al. 2006, MNRAS, 373, 397
Sharma, P., McCourt, M., Parrish, I. J., & Quataert, E. 2012a, MNRAS, 427, 1219
Sharma, P., McCourt, M., Quataert, E., & Parrish, I. J. 2012b, MNRAS, 420, 3174
Sharma, P., Parrish, I. J., & Quataert, E. 2010, ApJ, 720, 652
Singh, A., & Sharma, P. 2015, MNRAS, 446, 1895
Soker, N., White, R. E., III, David, L. P., & McNamara, B. R. 2001, ApJ, 549, 832
Sternberg, A., Pizzolato, F., & Soker, N. 2007, ApJL, 656, L5
Stone, J. M., & Norman, M. L. 1992, ApJS, 80, 753
Sun, M. 2009, ApJ, 704, 1586
Tombesi, F., Sambruna, R. M., Reeves, J. N., et al. 2010, ApJ, 719, 700
Tremblay, G. R., O'Dea, C. P., Baum, S. A., et al. 2012, arXiv:1205.2373
Vernaleo, J. C., & Reynolds, C. S. 2006, ApJ, 645, 83
Voigt, L. M., & Fabian, A. C. 2004, MNRAS, 347, 1130
Voit, G. M. 2005, RvMP, 77, 207
Voit, G. M. 2011, ApJ, 740, 28
Voit, G. M., Donahue, M., Bryan, G. L., & McDonald, M. 2015, Natur, 519, 203
Voit, G. M., Donahue, M., Bryan, G. L., & McDonald, M. 2015, 519, 203
Voit, G. M., Donahue, M., O'Shea, B. W., et al. 2015b, arXiv:1503.02104
Wagh, B., Sharma, P., & McCourt, M. 2014, MNRAS, 439, 2822
Werk, J. K., Proohaska, J. X., Tumlinson, J., et al. 2014, ApJ, 792, 8
Werner, N., Oonk, J. B. R., Son, M., et al. 2014, MNRAS, 439, 2291